SOLVING THE FORWARD PROBLEM OF ELECTRICAL SOURCE IMAGING BY APPLYING THE RECIPROCAL APPROACH AND THE FINITE DIFFERENCE METHOD

A THESIS SUBMITTED TO
THE GRADUATE SCHOOL OF NATURAL AND APPLIED SCIENCES
OF
MIDDLE EAST TECHNICAL UNIVERSITY

BY

SERCAN TAHA AHİ

IN PARTIAL FULFILLMENT OF THE REQUIREMENTS
FOR
THE DEGREE OF MASTER OF SCIENCE
IN
ELECTRICAL AND ELECTRONICS ENGINEERING

SEPTEMBER 2007

Approval of the thesis:

SOLVING THE FORWARD PROBLEM OF ELECTRICAL SOURCE IMAGING BY APPLYING THE RECIPROCAL APPROACH AND THE FINITE DIFFERENCE METHOD

submitted by **SERCAN TAHA AHİ** in partial fulfillment of the requirements for the degree of **Master of Science in Electrical and Electronics Engineering Department, Middle East Technical University** by,

Prof. Dr. Canan Özgen
Dean, **Graduate School of Natural and Applied Sciences** _____

Prof. Dr. İsmet Erkmen
Head of Department, **Dept. of EE, METU** _____

Prof. Dr. Nevzat G. Gençer
Supervisor, **Dept. of EE, METU** _____

Examining Committee Members:

Prof. Dr. Kemal Leblebicioğlu
Dept. of EE, METU _____

Prof. Dr. Nevzat G. Gençer
Dept. of EE, METU _____

Prof. Dr. Murat Eyüboğlu
Dept. of EE, METU _____

Asst. Prof. Dr. Yeşim S. Doğrusöz
Dept. of EE, METU _____

Prof. Dr. Ergin Atalar
Dept. of EE, Bilkent University _____

Date: _____

I hereby declare that all information in this document has been obtained and presented in accordance with academic rules and ethical conduct. I also declare that, as required by these rules and conduct, I have fully cited and referenced all material and results that are not original to this work.

Name, Last name : SERCAN TAHA AHİ

Signature :

ABSTRACT

SOLVING THE FORWARD PROBLEM OF ELECTRICAL SOURCE IMAGING BY APPLYING THE RECIPROCAL APPROACH AND THE FINITE DIFFERENCE METHOD

Ahi, Sercan Taha

Ms, Department of Electrical and Electronics Engineering

Supervisor: Prof. Dr. Nevzat G. Gençer

September 2007, 74 pages

One of the goals of Electroencephalography (EEG) is to correctly localize brain activities by the help of voltage measurements taken on scalp. However, due to computational difficulties of the problem and technological limitations, the accuracy level of the activity localization is not perfect and should be improved. To increase accuracy level of the solution, realistic, i.e. patient dependent, head models should be created. Such head models are created via assigning realistic conductivity values of head tissues onto realistic tissue positions.

This study initially focuses on obtaining patient dependent spatial information from T1-weighted Magnetic Resonance (MR) head images. Existing segmentation algorithms are modified according to our needs for classifying eye tissues, white matter, gray matter, cerebrospinal fluid, skull and scalp from volumetric MR head images. Determination of patient dependent conductivity values, on the other hand, is not considered as a part of this study, and isotropic conductivity values anticipated in literature are assigned to each segmented MR-voxel accordingly.

Upon completion of the tissue classification, forward problem of EEG is solved using the Finite Difference (FD) method employing a realistic head model. Utilization of the FD method aims to lower computational complexity and to simplify the process of mesh creation for brain, which has a very complex boundary. Accuracy of the employed numerical method is investigated both on Electrical Impedance Tomography (EIT) and EEG forward problems, for which analytical solutions are available. The purpose of EIT forward problem integration into this study is to evaluate reciprocal solution of the EEG forward problem.

Keywords: Magnetic Resonance Imaging, Segmentation, EEG Forward Problem, Reciprocity, Finite Difference Method

ÖZ

ELEKTRİKSEL KAYNAK GÖRÜNTÜLEME İLERİ PROBLEMİNİN KARŞITLILIK YAKLAŞIMI İLE SINIRLI FARKLAR YÖNTEMİ KULLANILARAK ÇÖZÜLMESİ

Ahi, Sercan Taha
Yüksek Lisans, Elektrik ve Elektronik Mühendisliği Bölümü
Tez Yöneticisi: Prof. Dr. Nevzat G. Gençer

Eylül 2007, 74 sayfa

Elektroensefalografi (EEG)'nin amaçlarından biri, kafaderisi üzerinden kayıt edilmiş voltaj ölçümleri ile beyin aktivitelerinin konumlarını doğru bir şekilde belirlemektir. Fakat problemin işlemsel zorlukları ve teknik sınırlar nedeniyle kaynak konumlandırmanın doğruluk oranı yeterli değildir ve iyileştirilmelidir. Çözümün doğruluk oranını artırmak için gerçekçi, yani hastaya bağlı kafa modellerinin oluşturulması gerekmektedir. Gerçekçi kafa modellerinin oluşturulması hastaya ait dokuların konum tespiti ardından doku iletkenlik değerlerinin uygun ilgili noktalara tayin edilmesiyle olur.

Bu çalışma öncelikle T1-ağırlıklı Manyetik Rezonans (MR) görüntülerinden hasta kafasına ait konumsal doku bilgisinin bulunmasına odaklanır. Halihazırdaki görüntü işleme teknikleri ihtayaçlar uyarınca şekillendirilerek göz, beyaz madde, gri madde, serebrospinal sıvı, kafatası ve kafaderisi hacimsel MR kafa görüntülerinden bolütlenmiştir. Hastaya bağlı iletkenlik değerlerinin belirlenmesi ise bu çalısmanın bir parcası olarak görülmemiş, literatürdeki izotropik

değerler dokulara uygun olarak atanmıştır.

Doku bölütlenmesi ardından EEG ileri problemi Sınırlı Farklar yöntemi ile gerçekçi bir kafa modeli kullanılarak çözülmüştür. Sınırlı Farklar yönteminin kullanımı ile, işlemsel karmaşayı kaldırmak ve çok girintili bir yüzeye sahip olan beyin üzerinde ağ yaratma işlemini kolaylaştırmak amaçlamaktadır. Tercih edilen sayısal modelin doğruluk oranları Elektrik Empedans Görüntüleme (EIT) ve EEG ileri problemleri üzerinde test edilmiştir. EIT ileri probleminin bu çalışmaya dahil edilmesindeki amaç EEG ileri probleminin resiprokal çözümünü değerlendirmektir.

Anahtar Kelimeler: Manyetik Rezonans Görüntüleme, Bölütleme, EEG İleri Problemi, Sınırlı Farklar Yöntemi

Tuğba, Naciye ve Vedat Ahi'ye itafen ...

ACKNOWLEDGMENTS

I would like to express my deepest gratitude to my supervisor Prof. Dr. Nevzat G. Gençer for his technical and non-technical guidance throughout this study. Working with Prof. Dr. Gençer has been a great privilege and a great experience.

I would also wish to express my admiration for each crew of the Biomedical Research Group, especially for Koray Özdal Özkan, Volkan Emre Arpınar, Doğa Gürsoy and Yoldaş Ataseven. Their friendship and assistance has been so unique that one can feel it even from thousands of kilometers away.

TABLE OF CONTENTS

LIST OF TABLES

LIST OF FIGURES

CHAPTER 1

INTRODUCTION

Brain communicates with the rest of the body by so-called action potentials sent via neurons. Information propagates in the form of electrical signals, and these electrical signals cause potential differences throughout the scalp. Potential distribution on the scalp caused by the electrical activities inside brain is measured by Electroencephalography (EEG). One of the major aims in measuring and monitoring this distribution is to localize sources of neuronal activities [1].

Since the measurement is realized by a limited number of electrodes placed on the scalp, the spatial resolution of measurements is quite low. However, the temporal resolution depends on the limits of the signal acquisition device, and this enables us to examine neural processes on millisecond time scales [1].

Finding locations and strengths of the unknown sources is called *inverse problem*. The inverse problem is an ill-posed problem, i.e. different activity patterns may create the same voltage distribution on the scalp. Therefore, some restrictions should be imposed to obtain a solution [2]. To solve the inverse problem of EEG, one should also be able to solve the *forward problem*, which is calculating potential distribution on scalp given a geometry, activity location and activity strength. However, having an extremely complex geometry, human head causes a major difficulty in this task. In the earliest studies, researchers have assumed a spherical geometry for human head and solved the forward problem analytically. Comparing EEG source localization errors of spherical and realistic head models, it is concluded that realistic models are

necessary for better localization [3, 4, 5].

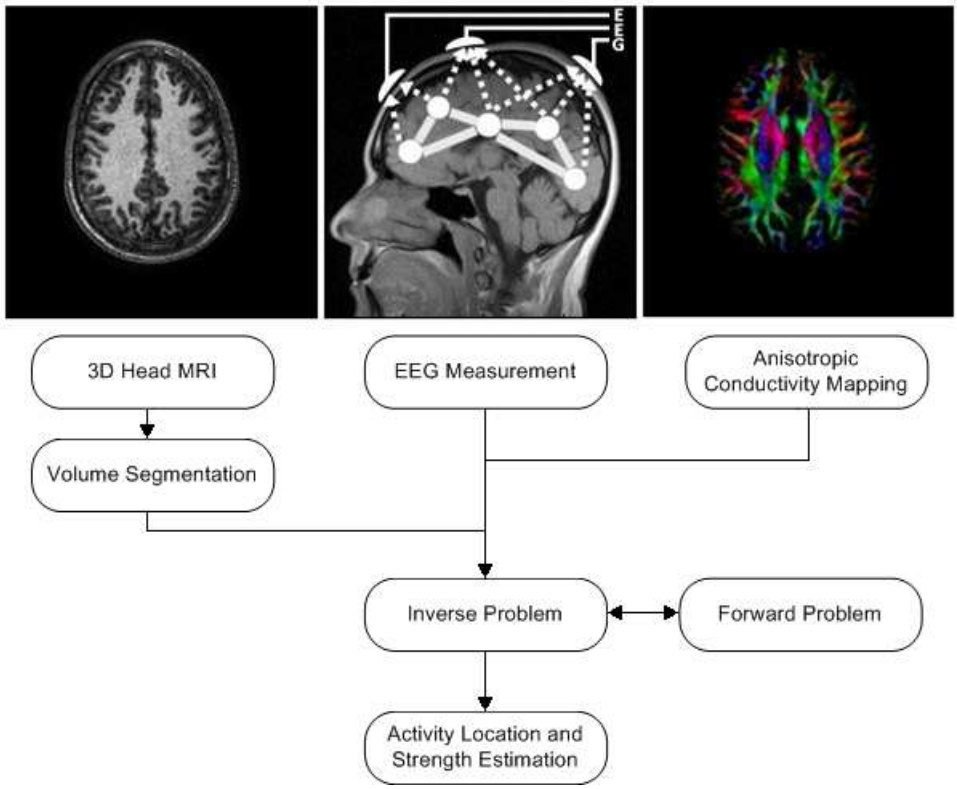

Figure 1.1: Flowchart of an ideal electrical source localization process.

Figure 1.1 describes an ideal EEG source localization scheme. This scheme is composed of realistic structural information obtained through Magnetic Resonance Imaging (MRI), realistic anisotropic conductivity distribution obtained through Diffusion Tensor Imaging (DTI) and electrical activity pattern obtained through high channel EEG monitoring. Segmenting MRI data into a known number of tissues, assigning them patient dependent conductivity values and incorporating this information into the forward problem forms the basics of an ideal source localization scheme. Usually such a scheme is simplified by using single pulse sequence MRI, whose details will be explained later in this chapter, and by ignoring tissue conductivity variation among patients. In this study, we also follow this simplified model and employ T1-weighted MRI data along with conductivity values determined in the previous studies.

Solving EEG forward problem using realistic head models requires numerical approaches like the Boundary Element Method (BEM), the Finite Element

Method (FEM) and the Finite Difference Method (FDM). Among these, the BEM provides relatively fast and accurate solutions [6, 7]. However, it does not allow anisotropic tissue conductivities, and it depends upon accurate mesh generation on complex geometry boundaries. On the other hand, FEM allows anisotropic tissue conductivities in calculations, but it also depends upon correct mesh generation in complex geometries. To improve accuracy, meshes should follow the three-dimensional geometry as much as possible. Composed of regular grids, FDM, on the other hand, greatly simplifies mesh creation process. Since our main concern in this study was to eliminate the requirement of complicated meshes, we investigated FDM by employing isotropic conductivity values.

Using the FDM in the EEG forward problem necessitates a high number of grids to improve accuracy. However, increasing the number of grids requires a corresponding increase in the memory consumption. In the third chapter of this study, we will question the efficiency of FDM in EEG forward problem in terms of accuracy, complexity and memory requirement. However, before that, we will first give some basic information about MRI in this chapter. Then we will present a 3D MRI data segmentation plan and introduce the details of each block in this plan in the next chapter.

1.1 Magnetic Resonance Imaging

Magnetic Resonance Imaging (MRI) is a non-invasive imaging modality, by which it is possible to visualize tissues by different intrinsic properties. Those intrinsic properties being visualized are proton density (PD), which is the concentration of hydrogen atoms per unit volume, the longitudinal relaxation time constant (T1), and the transverse relaxation time constant (T2).

The contrast in MR images can be adjusted by changing pulse sequence parameters. These parameters control the number, strength, shape, and timing of the RF and gradient pulses. The repetition time (TR), which is the time interval between two consecutive 90 degree RF pulses, and the echo time (TE), which is the time interval between the stimulating RF pulse and the

corresponding echo signal, are the most influential parameters.

The most common pulse sequences are the PD-weighted, T1-weighted, and T2-weighted sequences. If the data acquisition parameters are chosen such that the proton density of tissues gains dominance, the number of protons per unit volume determines the signal received. The higher the number of protons in a given unit of tissue, the greater the transverse component of magnetization, and the brighter the signal on the proton density contrast image. Conversely, the lower the number of protons in a given unit of tissue, the less the transverse magnetization and the darker the signal on the proton density image. If the data acquisition parameters are chosen such that T1 and T2 relaxation time constants of tissues gain dominance, the relaxation process of a spin system following the application of a stimulation is characterized in the reconstructed images.

Although each of these weighting provides different tissue contrast, T1-weighting became the de facto standard of the Neuroimaging community for brain segmentation and cortical surface extraction. The reason why most groups do not rely on dual-echo spin echo (i.e., PD- and T2-weighted) volumes [24] is that acquisition time is longer, signal-to-noise ratio (SNR) is reduced, the risk of head movement is higher, and intensity non-uniformity is more significant.

The last point that should be stressed about MRI is the low water content of skull, and consequently low MRI signal obtained from that region. The decrease in MRI signal level at skull regions causes a major problem in isolating the skull from air regions. The two common methods to overcome this problem is expanding and smoothing the brain surface obtained from T1-weighted MR images [51], and employing CT images [5]. In this study, we segmented whole skull tissue by only T1-weighted MR images.

1.2 Purpose of the Thesis

(1) *Segmentation*: One goal of this study is to create a modular software to segment head tissues from MR images. The modularity is necessary, because

identification of each tissue type may require different approaches, and if in the future a new method is developed exclusively for some tissues, then the developed method should easily be adapted into the whole segmentation process.

(2) *Finite Difference Method as a numerical solver*: Boundary Element Method (BEM) and Finite Element Method (FEM) are the two most common methods in the solution of EEG forward problem. Finite Difference Method (FDM), on the other hand, is usually not preferred due to its high memory requirement and low accuracy rate. Another goal of this study is to implement an FDM model and to investigate its computational complexity, memory requirement and accuracy.

(3) *Reciprocal approach in the forward problem solutions*: Source localization may be performed in a direct way by successively solving the forward problem of EEG, or in an indirect way by employing the theory of reciprocity, whose details will be given at the third chapter. Previous studies [47, 54] showed that reciprocal approach is a fast technique for source localization, as it requires only a small number of electric field solutions. Therefore, the last goal of this study is to incorporate the reciprocal approach into the forward problem by employing the developed FDM model.

1.3 Significance of the Thesis

(1) To be able to perform MR image segmentation accurately, existing algorithms are modified according to our needs, a modular head MRI segmentation scheme is constructed (Figure 2.1), and each module is implemented by MATLAB ®. Although there are different segmentation software packages available, they usually specialize in some head structures, and therefore researchers in the electrical source localization community need to use different packages simultaneously for creating their problem geometry. Moreover, electrical source localization community does not deeply interested in all brain structures, as some of those structures have similar conductivity values. In-

stead, the structures with different conductivities and with significant amount of volumes are of major importance. Our software package presents a solution, or at least a solution model, for the needs of electrical source localization studies.

(2) An accurate Finite Difference (FD) model [55] is implemented, its computational power requirement and its precision are investigated. Although there are some studies evaluating the implemented model [57], to our knowledge, the feasibility of the model is not questioned as exclusively as in this study.

(3) Reciprocal approach is incorporated into the forward problem and its accuracy level is tested. The test results are compared with the ones of the direct approach (Table 3.6 and 3.7). The comparison led us to the critical decision of employing the reciprocal approach and the implemented FD model into our laboratory's future source localization research. Moreover, although there are studies that employ similar models with the Reciprocal Approach [58], to our knowledge, the accuracy level of the model on the Reciprocal Approach is not evaluated before.

1.4 Thesis Outline

This thesis is divided into four chapters. In the first chapter, an introduction about the study and basics of Magnetic Resonance Imaging (MRI) are given. The purpose of the study is also included here. In the second chapter, methods for processing the Magnetic Resonance images are summarized and details about the general scheme followed are presented. The accuracy rate of the applied procedure is given for brain extraction, intensity non-uniformity correction and brain tissue identification methods. The literature survey about each segmentation block is presented accordingly. In the third chapter, EEG forward problem is investigated and the FDM is validated. Finally in the last chapter, conclusions and remarks of this work are stated.

CHAPTER 2

SEGMENTATION

2.1 Introduction

Segmentation of medical images, i.e. classifying tissues into subsets according to some predefined criteria, is a vital step for source localization research. Structural information coming from segmentation of medical images obtained via different imaging modalities, such as Magnetic Resonance (MR) or Computerized Tomography (CT), is mounted into the electro-magnetic problem of source localization. What is mounted into the problem is the position dependent conductivity values. In this study, we acquired position information using only MR modality. A T1-weighted MR volume is segmented into scalp, skull, cerebrospinal fluid (CSF), gray matter (GM), white matter (WM) and eye-ball tissues. An overview of the followed procedure is illustrated in Figure 2.1.

The whole segmentation procedure starts with extracting brain from the head volume. This process is called skull stripping and is of major importance due to the high conductivity value of CSF, which wraps the gray and white matters, and the low conductivity value of skull, which wraps the brain. Misclassifying brain boundaries causes erroneous results during source localization. Upon completion of brain segmentation, intensity non-uniformity is corrected. Correction of non-uniformity is a crucial step for segmenting brain tissues. Extracting the brain and correcting its intensity non-uniformity provides us with a comparatively simpler problem, which is brain tissue classification. After

solving this problem, we return to the classification of non-brain tissues. Being among non-brain tissues, eyes are extracted first. Following eye extraction, we segment scalp along with the fat tissue. Identifying the scalp tissue, we are able to determine the outer skull layer. Regarding the inner skull layer, it is assumed to be the same surface with the exterior of the cortex [5]. Based on this partially incorrect assumption a skull compartment is constructed, but it should be noted that even such a compartment constitutes a major correction in the creation of a volume conductor model.

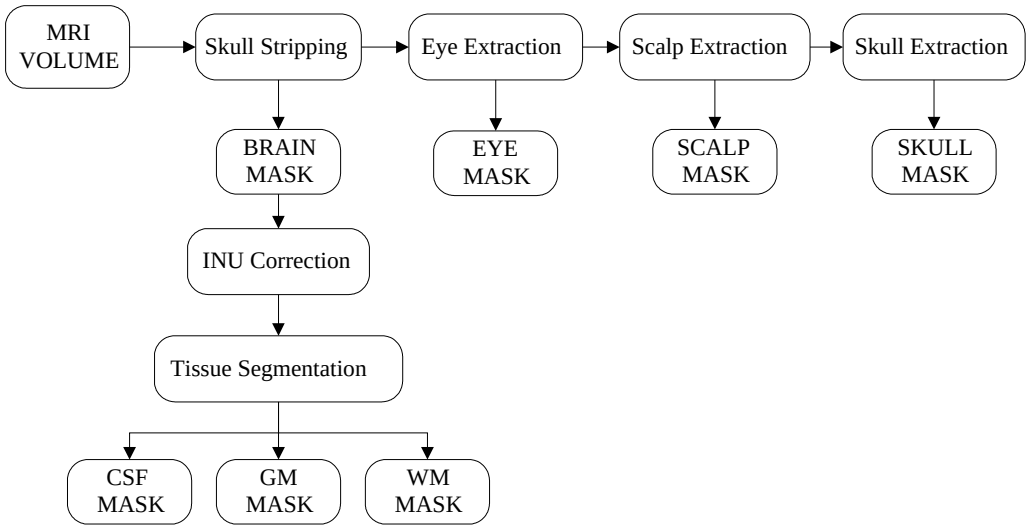

Figure 2.1: Flowchart of the head MRI segmentation algorithm.

In the following section, common methods used for segmenting MR images are given. The methods form the basics of the implemented algorithms, whose details are given in the "Segmentation of a 3D MRI Head Volume" section. We combined those common methods in a way that the tissue classification task is achieved with an acceptable amount of accuracy.

2.2 Background

2.2.1 Thresholding

Thresholding is an intensity based segmentation approach, in which selected intensity values partition the image domain into subsets, whose intersection is the empty set, and whose union is the whole image domain [8]. Partitioning is performed by classifying pixels with intensities above a threshold value into one subset and classifying pixels with intensities belove the threshold value into another one. The approach may be represented formally as follows [8]:

$$S_i = \{\mathbf{x} \in S_I : T_i \leq I(\mathbf{x}) < T_{i+1}\} \tag{2.1}$$

In Equation (2.1), S_I represents the image domain, $I(\mathbf{x})$ represents positional pixel intensity, and S_i represents one of the subsets formed by the threshold values T_i and T_{i+1}.

Although this approach is rather simple in nature, determining a proper value requires different perspectives. Methods for automatically specifying thresholds are generally based on image entropy, histogram concavity or prior knowledge [9]. Employing these methods, one can determine a proper threshold value automatically. However in the segmentation of MR images, thresholding is often used as an initial or intermediate step, because the method does not consider spatial characteristics and is very sensitive to irrelevant intensity variations throughout the image, which may be present in most MR images.

2.2.2 Region Growing

Region growing is a procedure of grouping pixels that show pre-defined similarities, such as gray level, color or texture [8]. The procedure starts with an automatic or manual seed assignment. Afterwards, pixels around the seed pixel are aggregated until there remains no other pixel that satisfies the pre-defined criteria.

Being a simple method like thresholding, region growing is generally used as an intermediate step in the segmentation of MR images, as well. The method

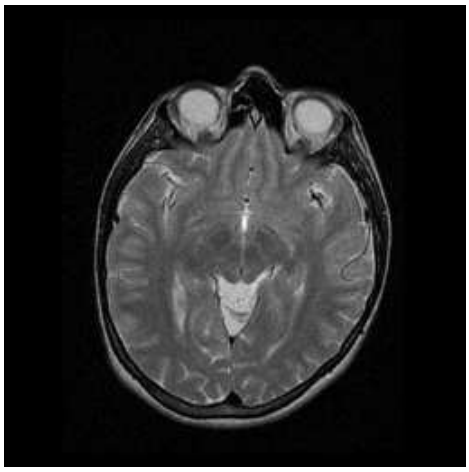

(a)

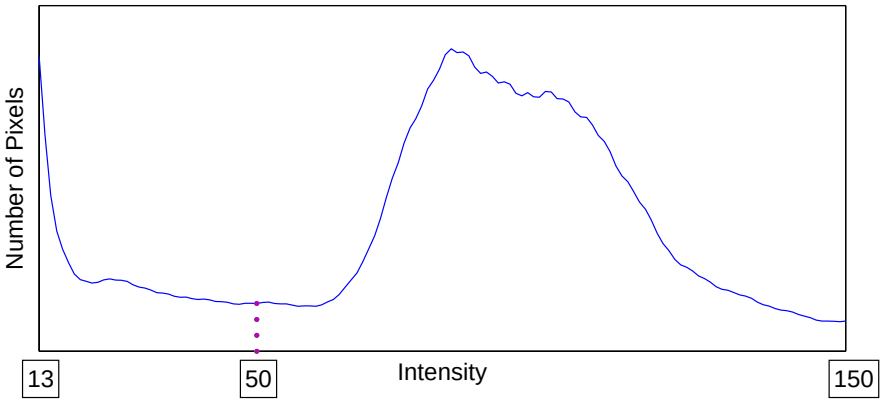

(b)

(c)

Figure 2.2: Thresholding applied on a T2-weighted MR image (a) Original image (b) Image histogram (c) Original image thresholded with an intensity value of 50

provides us with an easy approach to extract small and simple structures, such as eyes.

2.2.3 Laplacian of Gaussian Edge Detection

Edges are sudden changes in the image intensity. Separating continuous regions with discontinuities, edges contain important information about the physical extent of objects present in images. Therefore by identifying edges, the boundaries of objects are detected, and after carefully investigating those boundaries, image segmentation tasks may be fulfilled.

Being directly related to intensity changes, edges are detected by checking gradients along different directions in images. Calculation of gradients are realized by the Finite Differences. Since accuracy of the Finite Differences is easily affected by noise, edge detection procedures usually require noise filtering steps. Although causing losses on the edge strength and edge localization, filtering process is crucial (For observing the effect of the degree of Gaussian filtering on the final edge map you may look at Figure 2.3). Most methods overcome the edge strength loss problem by applying enhancement techniques.

Laplacian of Gaussian (LoG), also called as Marr & Hildreth, method uses a Gaussian filter to suppress the noise. Afterwards Laplacian operator is applied throughout the image to enhance edge strength. Lastly by checking zero-crossings, edges are determined.

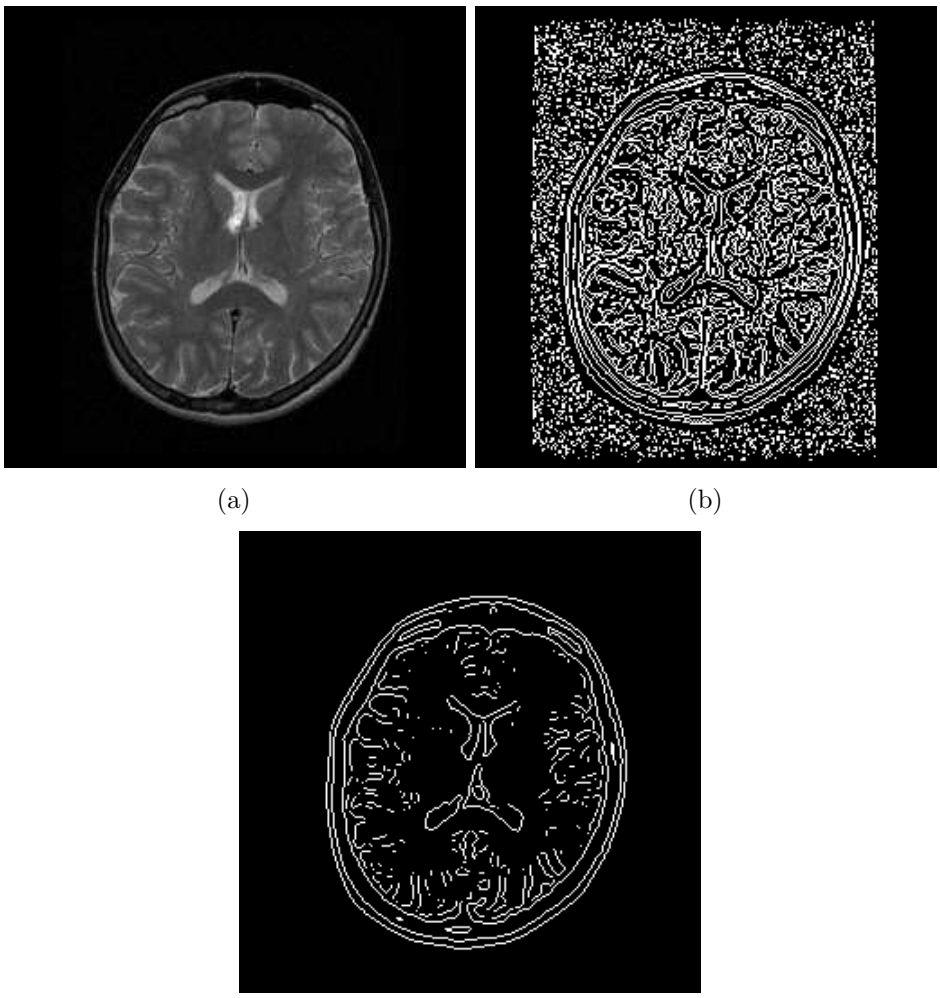

(a) (b)

(c)

Figure 2.3: Effect of Standard Deviation (σ) parameter on the identification of edges via Laplacian of Gaussian method. (a) Original T2-weighted MR image (b) $\sigma = 1$ (c) $\sigma = 2$

2.2.4 K-Means Clustering

K-means is an unsupervised clustering algorithm for classifying a data set, n, into a known number, c, of subsets according to a given criteria [14]. Usually, this criteria is selected as the Euclidean distance between data and subset centers, μ_i. The algorithm is initialized by assigning each member of the data set to a subset randomly. Then, corresponding cluster centers are calculated by simply finding the mean of subset members. Afterwards, the distance between each data and these centers is computed, and each data is reassigned to the closest subset. Continuing in this way, an iterative procedure is generated. Iterations continue until there is no change in the subset centers (see Figure 2.4 for details).

Being an unsupervised clustering algorithm, K-means provides the ability to perform segmentation tasks without any training data. However, the algorithm does not incorporate spatial information into consideration, and therefore it is susceptible to noise.

1: Knowing **n** and **c**, make an initial guess for $\mu_1, \mu_2, ..., \mu_c$
2: **while** There is a change in μ_i **do**
3: Classify **n** samples according to the nearest μ_i
4: Recompute μ_i by using newly classified samples
5: **end while**

Figure 2.4: K-means clustering algorithm [14].

2.2.5 Mathematical Morphology

Binary images can be modeled by point sets in 2D Euclidean space, E^2, and mathematical morphology is the application of specific set operators on these point sets [8]. Applied set operators have their roots in two basic operations, dilation and erosion, which are defined as follows:

$$\mathbf{A} \oplus \mathbf{B} \triangleq \{\mathbf{x} \in E^2 : \mathbf{x} = \mathbf{a} + \mathbf{b},\ \mathbf{a} \in \mathbf{A}\ and\ \mathbf{b} \in \mathbf{B}\} \tag{2.2}$$

$$\mathbf{A} \ominus \mathbf{B} \triangleq \{\mathbf{x} \in E^2 : \mathbf{x} \subset \mathbf{a}\ and\ \mathbf{x} + \mathbf{b} \in \mathbf{A}\} \tag{2.3}$$

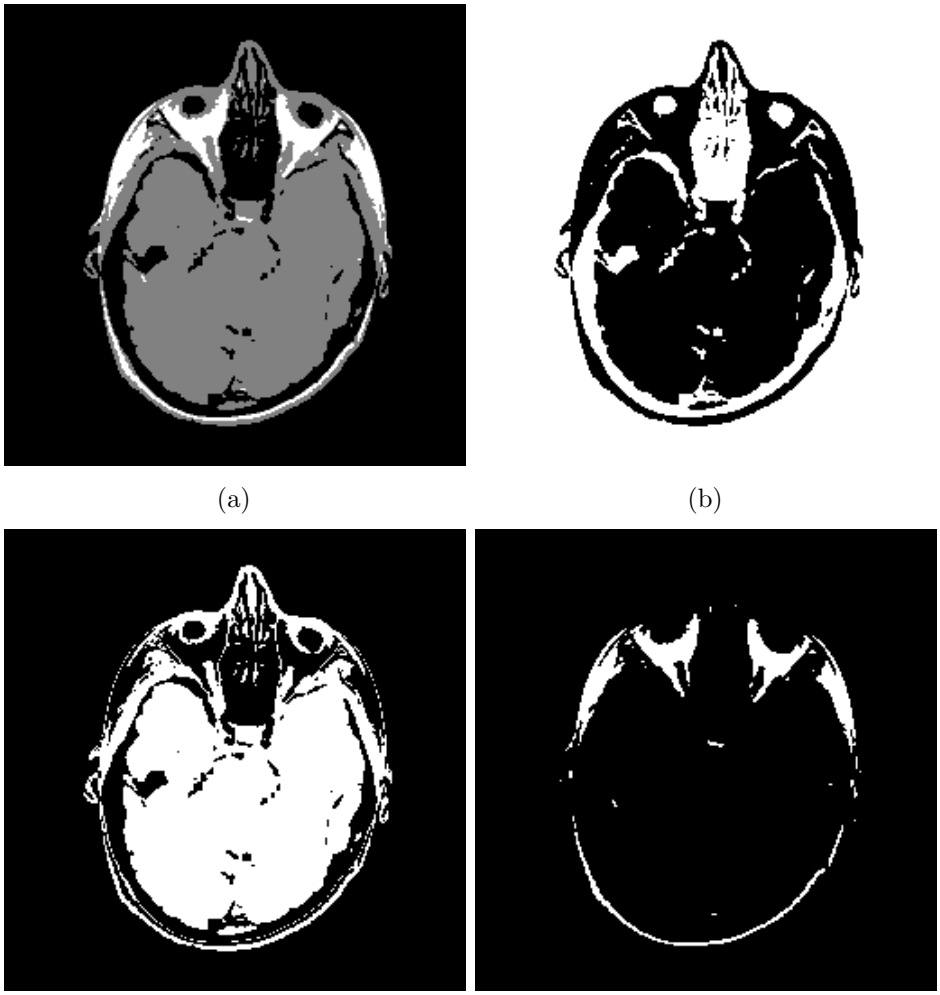

(a) (b)

(c) (d)

Figure 2.5: (a) K-means clustering of an MR volume into 3 clusters (b) 1. cluster (c) 2. cluster (d) 3. cluster

Based on dilation and erosion, new operations, such as opening and closing, may be derived. Opening, which tears thin connections apart and eliminates small regions, is application of erosion followed by dilation. Closing, which fills small gaps and merges narrow regions, is application of dilation followed by erosion.

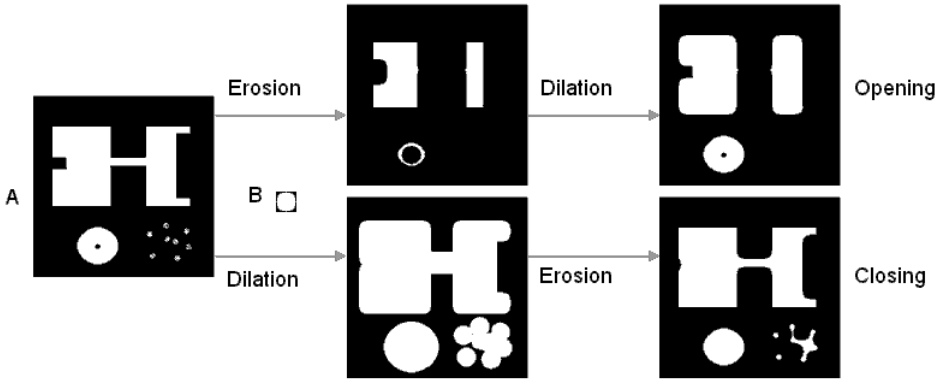

Figure 2.6: Dilation, erosion, opening and closing operations are illustrated. Slightly modified from [8].

2.2.6 Active Contour Models

Active contour models as introduced by Kass *et al.* [10] are deformable curves, or surfaces, localizing object boundaries present in images. The localization is realized by energy minimization. An energy functional is defined by a piecewise smooth curve equation and by chosen image properties. Upon defining the complete energy functional, the contour model is driven to the location where that functional takes the minimum value.

Mathematically speaking an active contour, or snake, is a curve defined as $\mathbf{v}(s) = (x(s), y(s))$, where x and y are coordinates of the points forming the curve. Both x and y depend on the parameter s, which takes values in the range of $[0, 1]$ based on the shape of the curve. Moreover, the energy functional to be minimized is defined as:

$$E = \int_0^1 \frac{1}{2}(\alpha|\mathbf{v}'(s)|^2 + \beta|\mathbf{v}''(s)|^2) + E_{ext}(\mathbf{v}(s))ds \tag{2.4}$$

In (2.4), α and β represent the weighting of active contour tension and rigidity during deformation process, respectively. $E_{ext}(\mathbf{v}(s))$ represents the chosen image properties, and it takes smaller values at places where those properties become significant. Lastly, $\mathbf{v}$' and $\mathbf{v}$" represent derivatives of $\mathbf{v}$, which is explained above.

A deformable contour that minimizes (2.4), satisfies the Euler equation, as well [10].

$$\underbrace{\alpha\mathbf{v}''(s) - \beta\mathbf{v}''''(s)}_{F_{int}} \underbrace{-\nabla E_{ext}}_{F_{ext}} = 0 \tag{2.5}$$

The solution to Equation (2.5), which may be considered as an equilibrium point of internal and external forces, is obtained iteratively. One more parameter, time, is added to $\mathbf{v}$ for this purpose.

$$v_t(s,t) = \alpha\mathbf{v}''(s,t) - \beta\mathbf{v}''''(s,t) - \nabla E_{ext} \tag{2.6}$$

Starting with an initial condition, $\mathbf{v}$(s,0), implementing derivatives with finite differences, and waiting for v_t(s,t) to converge, a solution to (2.4) is obtained.

The classical study of Kass *et al.* [10] offered image intensity, image gradients and curvature of level lines as possible image properties. Cohen [11] proposed a new force model by which the capture range of the active contour is increased. Moreover, while increasing its capture range, the overall performance of the contour is improved, as well. The new force model may simply be explained with the behavior of a balloon that is inflated with air. The inflation force provides the contour with the ability to pass through weak image features and stop at strong ones. However, as Xu and Prince [12, 13] noted, this new force model does not represent a solution to the problem with boundary concavities, where the active contours tend to generate erroneous results. Defining a new force field, namely Gradient Vector Flow, they increased the capture range and accuracy around concavities at the same time.

The vector field, $\mathbf{v}(x,y) = (u(x,y), v(x,y))$ that minimizes (2.7) is selected as a cure for the aforementioned problems associated with active contours.

$$E_{GVF} = \int\int \mu(u_x^2 + u_y^2 + v_x^2 + v_y^2) + |\nabla f|^2 |\mathbf{v} - \nabla f|^2 dxdy \qquad (2.7)$$

In Equation (2.7), (u,v) defines coordinate of a point in two dimensional space, u_x, u_y, v_x and v_y are directional derivatives of u and v, and $f(u,v)$ is the edge map.

2.2.7 Anisotropic Diffusion Filtering

2.2.7.1 Overview

Taking convolutions with Gaussian kernels is a common method for removing speckle noise present in most kind of images. The idea here is that to obtain coarser resolution images by applying a low-pass filter. Since the speckle, or salt and pepper, noise is composed of high-frequency random variations spread whole over the image, it is filtered after the application of the convolution. However, while removing high-frequency random variations, this filter smooths the edges, as well. Such kind of smoothing causes edge detection procedures generate erroneous results.

First proposed by Perona and Malik [15] and then applied by Gerig *et al.* [16] on MR images, anisotropic diffusion filters are adaptive filters that smooth images at varying levels. The level of smoothing is determined by how similar a pixel is to an edge. Determining the similarity of a pixel to an edge pixel is realized by measuring the gradient of the brightness function.

2.2.7.2 Mathematical Definition

Anisotropic diffusion equation is defined as:

$$I_{diff} = \nabla \cdot (c(\overline{x},t)\nabla I) = c(\overline{x},t)\nabla^2 I + \nabla c(\overline{x},t) \cdot \nabla I \qquad (2.8)$$

Here, $I(\overline{x},t)$ is the temporal intensity function. I_{diff} is the *diffused* temporal intensity function. They are "temporal", because as time passes, the diffusion propagates and the intensity functions take different values. $c(\overline{x},t)$, the conduction coefficient, is a function that controls the smoothing level of

the filter. Conduction coefficient is unknown and is to be determined by looking at the image gradient. Perona and Malik propose two different kinds of conduction coefficients:

$$c(\overline{x},t) = f(\| \nabla I \|) = e^{(-\frac{\|\nabla I(\overline{x},t)\|}{K^2})} \tag{2.9a}$$

$$c(\overline{x},t) = f(\| \nabla I \|) = \frac{1}{1+(\frac{\|\nabla I(\overline{x},t)\|}{K})^2} \tag{2.9b}$$

While these two equations have a common point, which is that they both decrease for increasing image gradients, they have different characteristics: (2.9a) preserves high-frequency edges and smooths out low-frequency ones; (2.9b) preserves wide regions and smooths out small ones. Shown in the above equation, "K" is the diffusion constant and a user selected parameter.

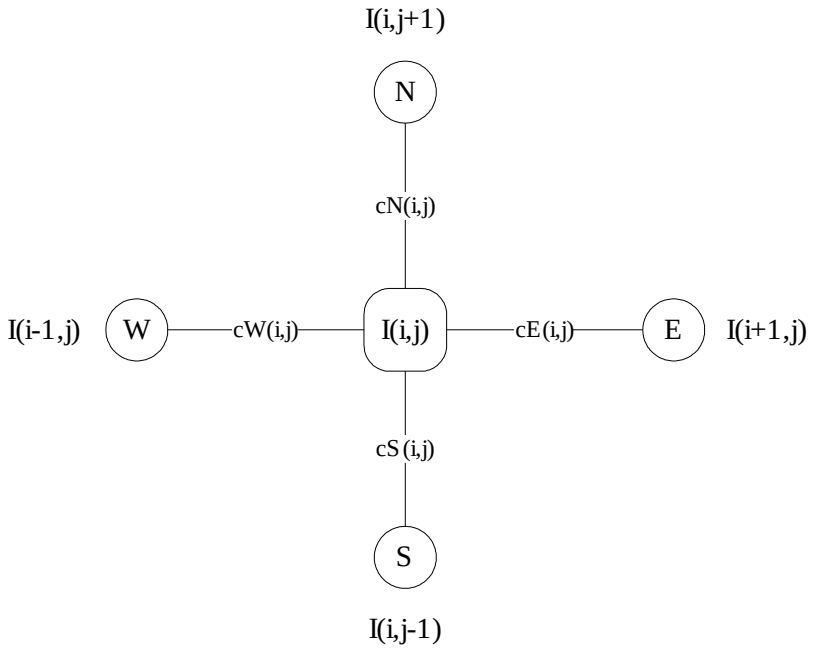

Figure 2.7: 5-stencil finite difference scheme for discretizing anisotropic diffusion equation. I(i,j) is the intensity of the center-pixel. I(i,j+1), I(i,j-1), I(i+1,j) and I(i-1,j) are surrounding pixels' intensities. cN, cS, cE and cW are directional coefficients defined by Equations (2.11) and (2.12).

2.2.7.3 2D Implementation

Implementation of anisotropic diffusion is realized by discretizing Equation (2.8). Discretization is performed in a 5-stencil Finite Difference scheme (see Figure 2.7):

$$I_{diff}^{t+1} = I_{diff}^{t} + \lambda[c_N \nabla_N I + c_S \nabla_S I + c_W \nabla_W I + c_E \nabla_E I]_{i,j}^{t} \tag{2.10}$$

In Equation (2.10), λ is the interval between two time instants and takes a value between 0 and 0.25 for stability of the scheme. "N", "S", "W" and "E" represent direction of the gradient, namely north, south, west and east. Selecting an internode spacing of unity, we may define the directional gradients as follows:

$$\begin{aligned} \nabla_N I_{i,j}^{t} &= I_{i,j+1}^{t} - I_{i,j}^{t} \\ \nabla_S I_{i,j}^{t} &= I_{i,j-1}^{t} - I_{i,j}^{t} \\ \nabla_W I_{i,j}^{t} &= I_{i+1,j}^{t} - I_{i,j}^{t} \\ \nabla_E I_{i,j}^{t} &= I_{i-1,j}^{t} - I_{i,j}^{t} \end{aligned} \tag{2.11}$$

Similarly:

$$\begin{aligned} c_{N\ i,j}^{t} &= f(\parallel \nabla_N I_{i,j}^{t} \parallel) \\ c_{S\ i,j}^{t} &= f(\parallel \nabla_S I_{i,j}^{t} \parallel) \\ c_{W\ i,j}^{t} &= f(\parallel \nabla_W I_{i,j}^{t} \parallel) \\ c_{E\ i,j}^{t} &= f(\parallel \nabla_W I_{i,j}^{t} \parallel) \end{aligned} \tag{2.12}$$

2.3 Segmentation of a 3D MRI Head Volume

2.3.1 Skull-Stripping

The procedure of isolating brain from extra-cranial tissues is called skull-stripping. The performance of this procedure depends on the age and diagnosis of the subject, type and resolution of MR images, and level of magnetic inhomogeneities in the MR magnets.

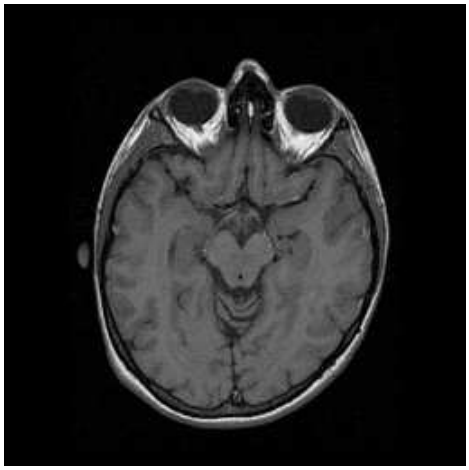

(a) Original image

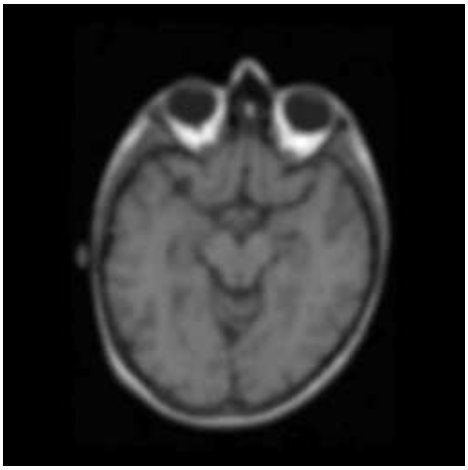

(b) Gaussian smoothing

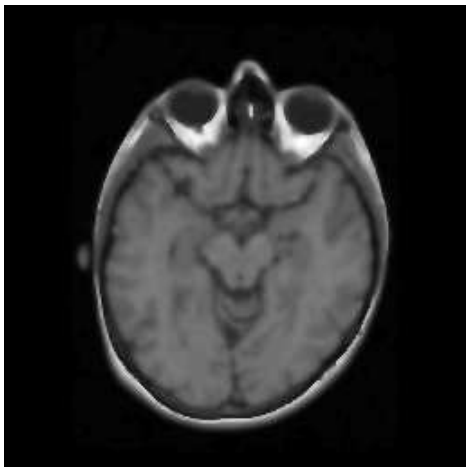

(c) Anisotropic filtering

Figure 2.8: Visual comparison of Gaussian and Anisotropic smoothing. In (b), the original 256x256 image is convolved with a 5x5 kernel. In (c), the original image is filtered anisotropically with a diffusion constant of 25 and an iteration number of 3.

Among the methods shown in Table (2.1), the one proposed by Shattuck *et al.* [33] is employed in this study, and a MATLAB ® software module is implemented. As shown in Figure 2.9, the whole procedure is mainly composed of four steps: In the first step, the original volume is smoothed by applying an anisotropic filter. During our experiments, we selected the diffusion constant as 25, and repeated the filtering for a total of three times. After the smoothing step, edges are identified by the help of Laplacian of Gaussian (LoG) method. LoG proposes to use a Gaussian operator to suppress noise and a Laplacian operator as edge enhancer. We selected the standard deviation as 0.62 and radius as two, which are used in the Gaussian operator, and we marked the voxels of the mask which were negative in the Laplacian of the filtered image as edges. In the third step, brain region is isolated. This is realized by morphological erosion with a 3D rhombus structure of radius one. Erosion separates some connections between brain and surrounding regions. A primitive brain mask is obtained by selecting the largest connected component. However due to erosion, it is rather corrupted. The obtain a better brain mask, the primitive one is dilated with again a 3D rhombus structure of radius one and holes in the interior regions are filled. Eroding with a 3D octagon structure of size two, the final brain mask is obtained. This procedure constitutes the last step of the algorithm.

Table 2.1: Literature on brain extraction.

Reference	**Method**
Ségonne *et al.* [17]	Hybrid
Atkins *et al.* [23]	Hybrid
Smith [18]	Deformable model
MacDonald *et al.* [20]	Deformable model
Shattuck *et al.* [33]	Edge detection
Tang *et al.* [21]	Edge detection
Ashburner *et al.* [30]	Atlas warping
Stokking *et al.* [19]	Intensity analysis
Lemieux *et al.* [22]	Intensity analysis

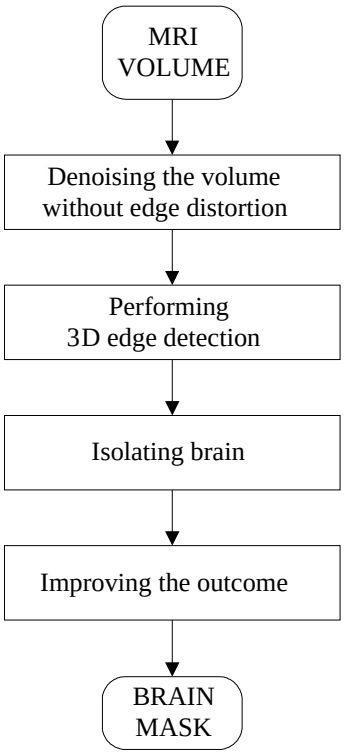

Figure 2.9: Flowchart of the skull-stripping algorithm, which is implemented by MATLAB ®.

2.3.2 Correction of Intensity Non-uniformity

The general model that describes the effect of intensity non-uniformity on MR images is as follows:

$$v(\overline{r}) = f(\overline{r}) \cdot u(\overline{r}) + n(\overline{r}) \tag{2.13}$$

In Equation (2.13), $v(\overline{r})$ is the corrupted MRI intensity with respect to position, $f(\overline{r})$ is the modulating non-uniformity field, $u(\overline{r})$ is the pure uncorrupted MRI intensity and lastly $n(\overline{r})$ is an additive noise, which is mostly assumed to have a Gaussian distribution [30, 33]. The additive noise is accepted to be statistically independent from $u(\overline{r})$ and is usually neglected.

The modulation field, $f(\overline{r})$, is assumed to vary slowly throughout the volume. This assumption prevents high tissue-intensity-contrast from being misclassified as the modulation function and makes it possible to decrease the computational cost by performing calculations only on subsamples [25, 33] or on the DCT coefficients [30] of the image.

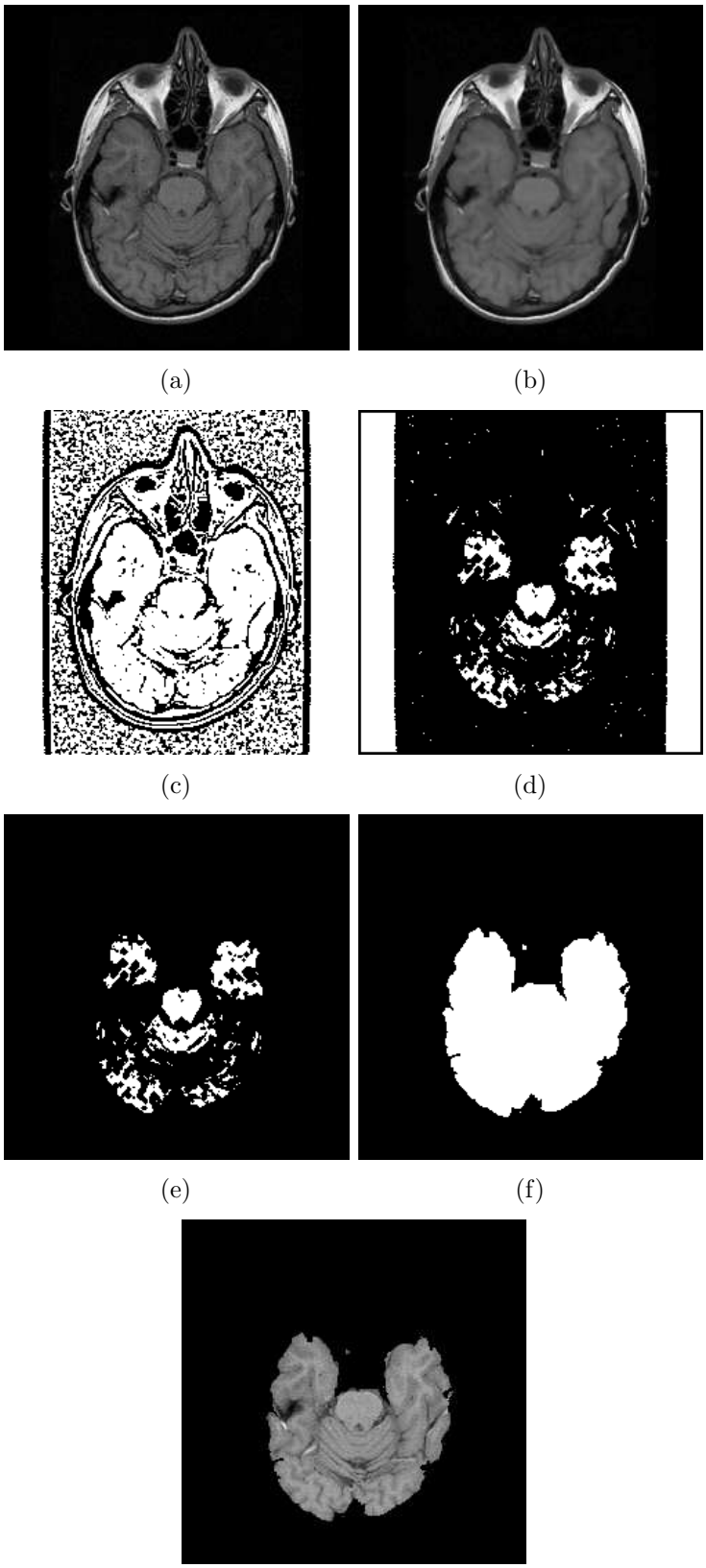

Figure 2.10: BSE steps: (a) Original volume, (b) Anisotropic filtering applied, (c) Modified LoG applied, (d) Erosion applied, (e) Largest connected component selected, (f) Modified closing applied, (g) Final volume

In this study, we employed the method of Ashburner *et al.* [30], in which it is assumed that the non-uniformity field has multi-normal distribution with a uniform mean and with a covariance matrix which is able to model smooth variations. A cost function is created based on this assumption, and the field is estimated by minimizing the sum of squared differences between original data and the chosen model.

2.3.3 Segmentation of Brain Tissues

Although segmentation of cortex tissues is an important process, due to the complex nature of the volume, due to the variable contrast level of MR images and due to noises peculiar to the MR protocol, a widely accepted method has not been developed yet. Proposed solutions to this problem is mostly based on statistical approaches. Some researchers have applied modified fuzzy clustering algorithms [32], some constructed Bayesian schemes [33, 34] and some developed modified finite mixture models [31].

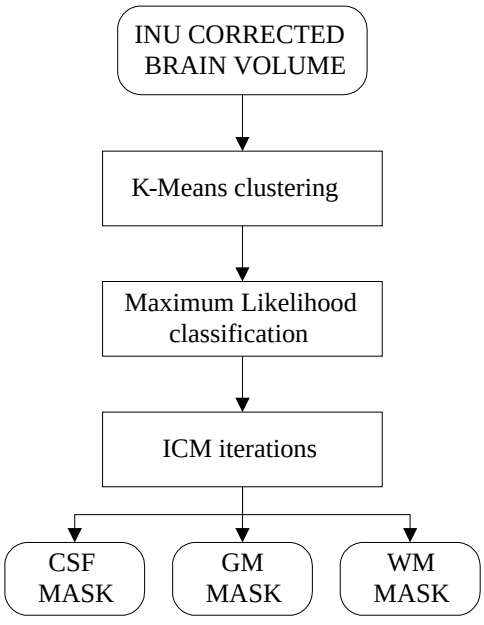

Figure 2.11: Flowchart of the brain tissue classification algorithm, which is implemented by MATLAB ®.

For obtaining piecewise constant tissue surfaces and for eliminating speckle noises in MR images, spatial penalty functions are added into the classification

algorithms [28], [36], [29]. If the neighbors of a voxel are all of the same tissue type, then it is not highly probable that the corresponding voxel is of another tissue type. This known fact is incorporated into the segmentation procedure with the help of penalty functions.

In our study, we employed a slightly modified version of Partial Volume Classifier (PVC) [33], where it is assumed that intensity non-uniformity is corrected beforehand, and the volume is composed of five classes: CSF, GM, WM, CSF/GM (CG), and GM/WM (GW). In the original method, there is one more type called as CSF/other, which represents non-cortex tissues like dura-matter. However, in our implementations that class is ignored. The probability density functions of all of these types are modeled as gaussian with mean μ, variance σ^2 and are represented by g(x;μ,σ). From the five classes assumed to be present in the volume, density functions of the three pure ones are modeled as:

$$p(x_k|\gamma) = g(x_k; \mu_\gamma, \sigma),\ \gamma \in \{CSF, GM, WM\} \tag{2.14}$$

and density functions of the remaining mixed-tissue classes are modeled as:

$$\begin{aligned} p(x_k|\gamma) &= \int_0^1 g(x_k; \alpha\mu_A + (1-\alpha)\mu_B, \sigma) d\alpha \\ &= \frac{1}{2(\mu_B - \mu_A)}[erf(\frac{x_k - \mu_A}{\sqrt{2}\sigma}) - erf(\frac{x_k - \mu_B}{\sqrt{2}\sigma})], \gamma \in \{CG, GW\} \end{aligned} \tag{2.15}$$

In Equation (2.15), erf(x) is equal to $\frac{2}{\sqrt{\pi}} \int_0^x e^{-t^2}\ dt$, $erf(0) = 0$, and $\mu_B > \mu_A > 0$.

Using these densities and the Bayes' formula, a maximum a posterior probability classifier is constructed. Bayes' formula states that a posterior probability is directly proportional to the product of likelihood and prior. The modified version of PVC differs from the original algorithm in the specification of "prior". Original algorithm defines the prior as follows:

$$p(\Lambda) = \frac{1}{Z}\ exp\left(-\beta \sum_{k \in N^3} \sum_{j \in N_k} \psi_{k,j} \delta(\gamma_k, \gamma_j)\right) \tag{2.16}$$

Here, $\Lambda = \{\gamma_1, \gamma_1 ... \gamma_{N^3}\}$. and Z represents a scaling constant. It provides us with the opportunity to construct a proper density function, whose integral between minus and plus infinities is equal to one. β represents the strength of the prior, N_k represents the D18 neighborhood, and δ is a function that returns -2 if labels "k" and "j" are identical, -1 if γ_k and γ_j have a common tissue type, and 1 if they don't have a common tissue type. This way, if the neighbors of a pixel are of the same class with itself, $-\beta \sum_{k \in N^3} \sum_{j \in N_k} \psi_{k,j} \delta(\gamma_k, \gamma_j)$ returns a positive value, and this increases the possibility of that pixel to belong to the current class, i.e., no update is necessary. This is the function that penalizes the speckle noise. The last variable, $\psi_{k,j}$, scales the penalization coefficients according to the distance between the k_{th} and j_{th} voxels, that is $\psi_{k,j}$ takes a of 1 if k_{th} and j_{th} voxels share a face, $\psi_{k,j}$ takes a of $\frac{1}{\sqrt{2}}$ if they share only an edge. PVC assumes same in-plane and out-of plane resolutions. However, usually this is not the case. Out-of plane resolution is mostly larger than the in-plane resolution. Therefore, our implementation addresses this fact by modifying the scale coefficients according to data resolution.

The Bayes' scheme is realized with iterated conditional modes (ICM) algorithm [26]. Before running the ICM algorithm, tissue labels are selected according to maximum likelihood classification. Then an iterative updating is initiated according to the following formula:

$$\gamma_k^{n+1} = argmax_\gamma [logp(x_k|\gamma_k^n) - \beta_1 \sum_{j \in N_k} \psi_{k,j} \delta(\gamma_k^n, \gamma_j) + \beta_2 \varphi(k)] \qquad (2.17)$$

Iteration continues until there is no change in the labeling of the tissues.

2.3.4 Segmentation of Eyes

Segmentation of eyes is the simplest one among the other tasks shown in Figure 2.1. This is due to their uniform shape and due to the existence of important information such as the approximate location and size of the structure.

Orientation of an object is identified with the line for which the sum of distances between each object point is minimum. The angle between this line,

which may also be defined as the medial axis of the object, and the x-axis is mathematically defined in Equation (2.18) [37] and shown as θ. In Equation (2.18), $I(x, y)$ represents the image intensity at (x,y) coordinate.

$$\begin{aligned} tan2\theta &= \frac{b}{a-c} \\ a &= \sum_x \sum_y x^2 I(x,y) \\ b &= 2\sum_x \sum_y xy I(x,y) \\ c &= \sum_x \sum_y y^2 I(x,y) \end{aligned} \tag{2.18}$$

By the help of medial axis and the line perpendicular to the medial axis, MR slices are divided into four regions individually. It is assumed that eyes are lateral spherical structures with around 12mm. of radius and located in the anterior side of the head. Based on these assumptions, each MR slice that includes brain is processed individually. On the frontal two regions, circular Hough transform is applied. Selecting the slice with the highest accumulator value provides us with the ability to determine a proper slice with reasonable eye area automatically. Determining the slice and seed locations for eyes, region growing algorithm is applied. Since MRI intensity of eye tissue is remarkably different from surrounding tissues no matter what the MRI weighting is, it is a straightforward and simple task to segment it by this method. Being dependent on intensity levels, region growing algorithm may not yield correct results. For decreasing disturbance of the noise on this process, we applied anisotropic filtering right at the beginning of this segmentation task.

2.3.5 Segmentation of Scalp and Skull

The procedure of scalp segmentation comprises two stages: isolation of head volume from background voxels followed by the identification of outer skull surface. The region between outer skull and outer scalp surfaces is deemed the scalp volume. Isolation of head volume from background voxels is a consider-

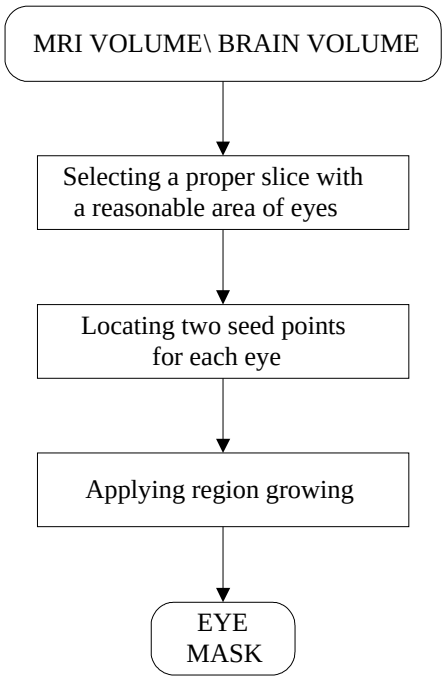

Figure 2.12: Flowchart of the eye-segmentation algorithm, which is implemented by MATLAB ®

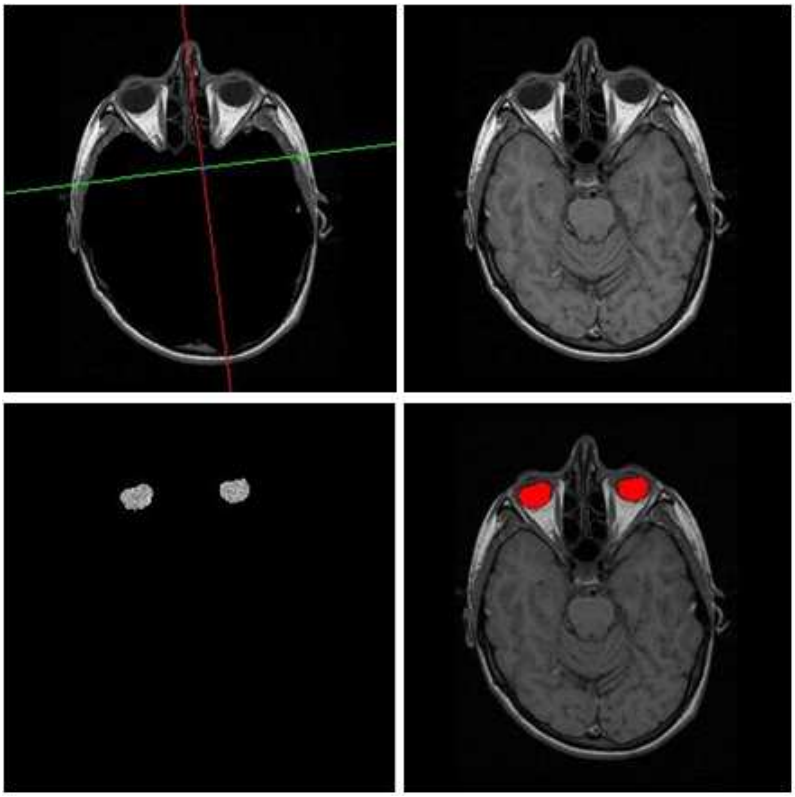

Figure 2.13: Illustration of the eye-segmentation procedure.

ably simple task, as the gray level change between foreground and background volumes is rather significant.

On the contrary to the outer scalp identification, segmentation of skull from MR images is an extremely difficult task because of the low signal level obtained from skull tissue. In other words, MR imaging modality does not provide us with satisfactory information about the spatial content of skull. Therefore in studies where high resolution information is not required, CT imaging is employed. High-resolution CT images may also be taken, yet in such cases subjects are exposed to X-rays for a long duration, which is mostly undesirable.

Publications focusing on skull segmentation solely from MR images are quite few. Among these, [38] tries to determine skull volume by region growing and 3D deformable models; [39] tries to fulfill this task by mathematical morphology, and lastly [40] estimates the surfaces by intensity clamping on T1-weighted and T2-weighted volumes from the same subject. Utilization of two different weighted volumes aims at distinguishing skull and CSF, which is dark in T1-weighted and bright in T2-weighted images. Skull, on the other hand, is generally dark in all type of MR images.

In our implementations, we followed methods proposed in [39]. The reason is the simplicity of mathematical morphology and our goal, which is segmenting whole volume by only T1-weighted images. Flowcharts, which are shown in Figure 2.16 and 2.17, summarize the whole procedure of finding outer scalp and outer skull regions. By estimating outer scalp region, will be able to eliminate background voxels. Eliminating background voxels, we will focus on the outer skull surface; and determining outer skull surface we will be able to extract scalp volume. Regarding the skull volume, we will make an important assumption that the outer brain surface represents the inner skull surface. From source localization point of view, this assumption doesn't create a major error, because the conductivity of air and skull are both quite low.

Identification of outer scalp surface starts with the estimation of two threshold values, namely T_{skull} and T_{scalp}. T_{skull} is the mean of voxels that are not

labeled as brain and have intensities above zero. T_{scalp} is the mean of voxels that are not labeled as brain and have intensities above T_{skull}.

Mathematically speaking:

$$T_{skull} = \frac{1}{s(V_{nb})} \sum_{k \in V_{nb}} I_k \tag{2.19}$$

$$T_{scalp} = \frac{1}{s(V_{ns})} \sum_{k \in V_{ns}} I_k \tag{2.20}$$

where,

$$V_{nb} = \{k : k \in V \setminus B, I_k > 0\} \tag{2.21}$$

$$V_{ns} = \{k : k \in V \setminus B, I_k \geq T_{skull}\} \tag{2.22}$$

Then, the procedure continues with thresholding:

$$V_{t_{scalp}} = \{k : k \in V, I_k \geq T_{scalp}\} \tag{2.23}$$

$V_{t_{scalp}}$, which is obtained by thresholding initial MRI volume with T_{scalp}, may include some background voxels due to noise, or exclude some CSF voxels due to low intensity level. Moreover after thresholding, some cavities around sinus and ear canal regions form. These cavities constitute a major difficulty in the segmentation process, because they detach connected structures. Dogdas [39] proposes a modified closing operation to reduce the negative effect of these cavities. The difference between the usual and modified closing operations is the application of hole filling operation between dilation and erosion operations. They employ a O_2 type structuring element for this purpose.

$$V_{t\_scalp\_filled} = V_{t\_scalp} \odot O_2 \tag{2.24}$$

$V_{t\_scalp\_filled}$, which is obtained by the application of modified closing operation, comprises a number of connected components. Choosing the largest one among these components, we obtain the outer boundary of the scalp.

Identification of the outer skull surface starts with the application of anisotropic filter followed by a thresholding procedure. Filtered MRI volume is reversely

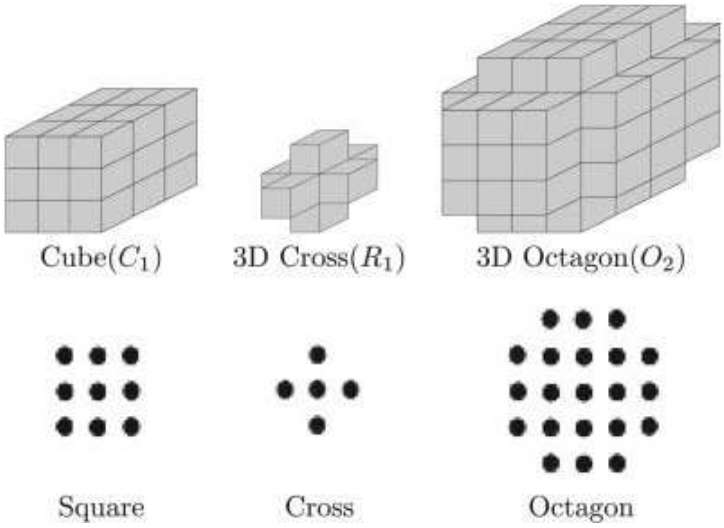

Figure 2.14: Structuring elements used in the scalp and skull segmentation processes [39].

thresholded with T_{skull} and V_{t_skull} is obtained. However, it is highly possible that this volume excludes some dark regions of skull and CSF. Thus to widen the initial skull volume estimation, the brain volume is dilated after removing brainstem, and union of these two sets are taken, producing V_{u_out}. Afterwards intersection of V_{u_out} is taken with a modified head volume. The volume is modified such that ears and nose are removed. This step is quite important, because it is not possible to distinguish regions filled with air by simply thresholding. Taking intersection, the resultant volume is composed of a number of connected components. Selecting the largest component does not complete the procedure. After this point, some other structures such as eye sockets should be eliminated. To do this, previously modified head volume is used. Closing the largest connected component, $V_{largest}$, with O_4 and taking their intersection provides us with a very rough estimation of the outer skull surface.

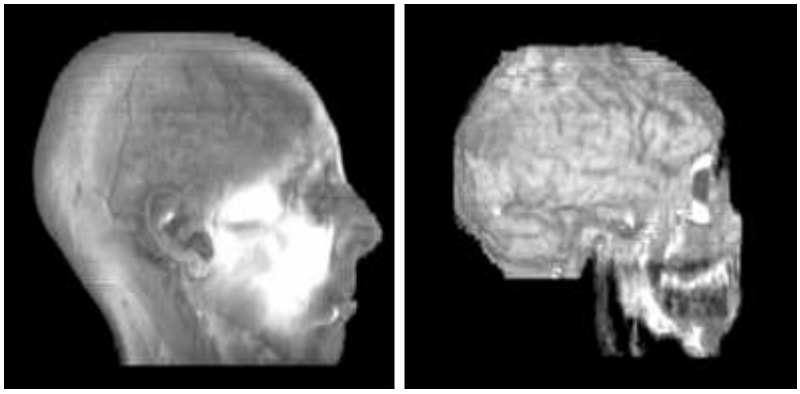

Figure 2.15: Extracted scalp and skull

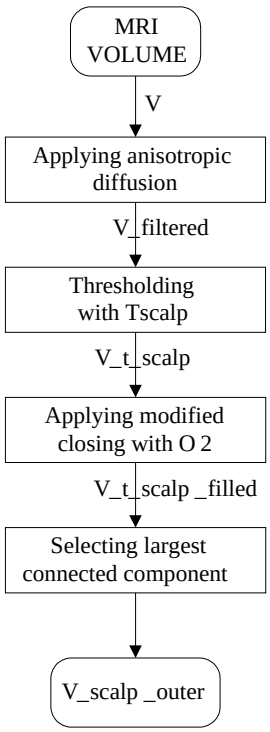

Figure 2.16: Flowchart of scalp segmentation algorithm, which is implemented by MATLAB ®

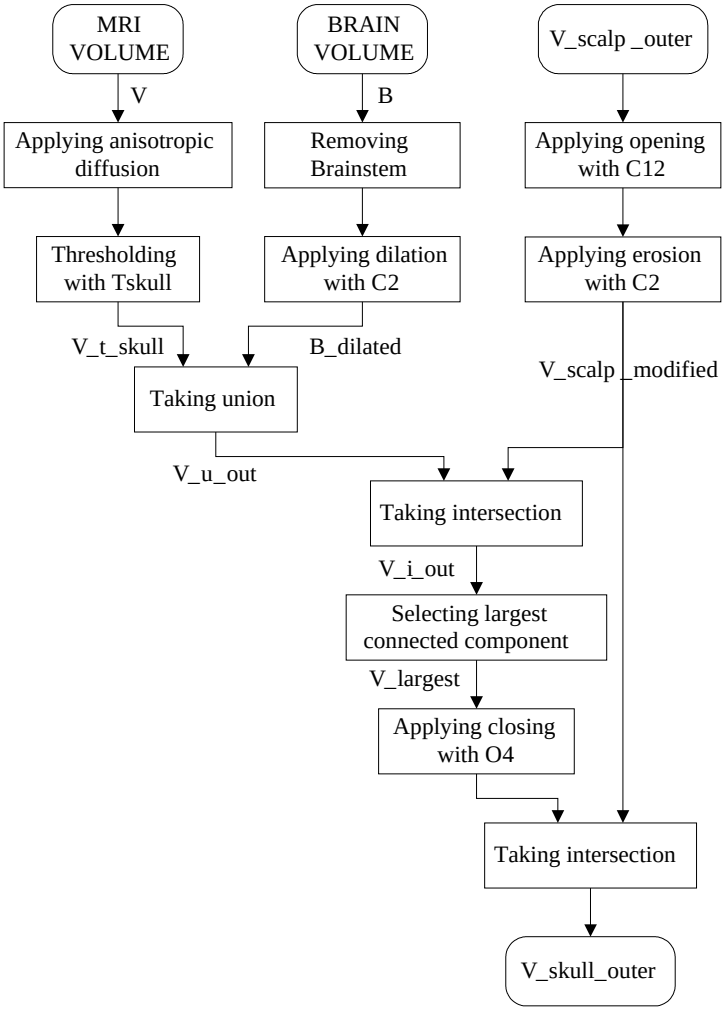

Figure 2.17: Flowchart of skull segmentation algorithm, which is implemented by MATLAB ®

2.4 Quantitative Evaluation of the Segmentation Algorithm

The McConnell Brain Imaging Centre at Montreal Neurological Institute provides research community with an MRI simulator through which it is possible to obtain head phantoms acquired at different pulse parameters [41], [42]. Using this simulator, it is possible to add noise and intensity non-uniformity on MR images at desired levels. The levels of noise set for evaluation are %0, %1, %3, %5 and %7. The percentage is determined with respect to intensity of the brightest tissue in volume. The levels of intensity non-uniformity selected for evaluation are 0, 20 and 40. These numbers represent some specific ranges determined by the developers of the simulator.

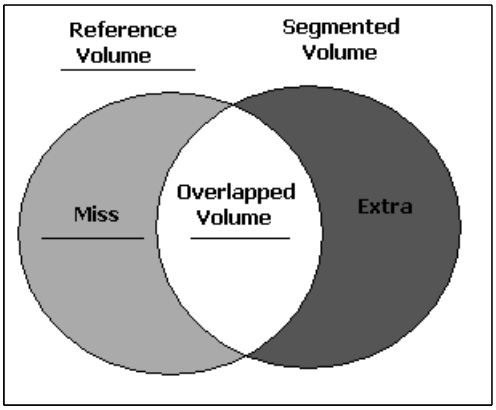

Figure 2.18: Quantitative evaluation is performed by calculating missed, extra segmented and overlapped volumes.

The measures used throughout the evaluation process are %O (percentage of overlapped volume), %E (percentage of extra volume), %M (percentage of missed volume), Similarity Index (SI) [27], [19] (see Figure 2.18) and Relative Difference Measure [49]. Mathematical definitions of the first 4 measures are given at Equations (2.25a) to (2.25d). Lastly, the evaluation results are given in Tables (2.2), (2.3) and (2.4).

$$\mathrm{E} \triangleq \frac{\text{Extra}}{\text{Reference Volume}} \text{ x } 100 \tag{2.25a}$$

$$\mathrm{M} \triangleq \frac{\text{Miss}}{\text{Reference Volume}} \text{ x } 100 \tag{2.25b}$$

$$\mathrm{O} \triangleq \frac{\text{Overlapped Volume}}{\text{Reference Volume}} \text{ x } 100 \tag{2.25c}$$

$$\mathrm{SI} \triangleq \frac{2 \text{ x Overlapped Volume}}{\text{Reference Volume + Segmented Volume}} \tag{2.25d}$$

Table 2.2: Quantitative analysis of the implemented brain segmentation module.

MRI	**%O**	**%E**	**%M**	**SI**
0n00rf	92.51	2.35	7.49	0.950
0n20rf	92.28	2.01	7.72	0.950
0n40rf	90.15	0.99	9.85	0.943
1n00rf	92.16	1.83	7.84	0.950
1n20rf	88.52	0.44	11.48	0.937
1n40rf	88.70	0.47	11.31	0.938
3n00rf	91.86	1.62	8.14	0.950
3n20rf	88.45	0.57	11.55	0.936
3n40rf	88.47	0.50	11.53	0.936
5n00rf	90.36	1.02	9.64	0.944
5n20rf	90.52	1.29	9.48	0.944
5n40rf	90.78	1.40	9.22	0.945
7n00rf	88.33	0.56	11.68	0.935
7n20rf	88.41	0.58	11.59	0.936
7n40rf	89.15	0.85	10.86	0.938
Mean	**90.04**	**1.10**	**9.96**	**0.942**

Table 2.3: Quantitative analysis of intensity non-uniformity correction module.

MRI	**%RDM**
1n20rf	0.73
1n40rf	1.44
3n20rf	0.73
3n40rf	0.95
5n20rf	1.34
5n40rf	1.32
7n20rf	2.33
7n40rf	2.03
Mean	**1.36**

Table 2.4: Quantitative analysis of the implemented brain tissue segmentation module.

	CSF			**GM**			**WM**		
MRI	**%O**	**%E**	**SI**	**%O**	**%E**	**SI**	**%O**	**%E**	**SI**
0n00rf	98.36	2.52	0.979	95.75	0.89	0.974	99.72	4.30	0.978
0n20rf	97.19	3.00	0.971	94.13	3.20	0.954	97.26	6.20	0.956
0n40rf	95.79	5.57	0.951	91.23	8.28	0.915	91.25	8.66	0.913
1n00rf	98.17	2.62	0.978	96.16	1.18	0.975	99.43	3.70	0.979
1n20rf	97.28	3.38	0.970	94.26	3.45	0.953	96.88	5.82	0.956
1n40rf	95.93	5.98	0.950	90.49	7.93	0.912	91.63	9.42	0.911
3n00rf	97.15	3.64	0.968	94.04	2.45	0.957	98.30	5.97	0.962
3n20rf	96.37	4.16	0.961	93.29	4.44	0.944	96.07	6.69	0.948
3n40rf	94.94	6.35	0.943	89.26	8.47	0.903	91.46	10.88	0.904
5n00rf	95.65	5.16	0.953	91.72	3.69	0.939	97.45	8.23	0.948
5n20rf	94.73	5.13	0.948	90.97	5.36	0.927	95.73	9.25	0.934
5n40rf	93.64	7.18	0.933	88.78	10.13	0.893	89.95	11.05	0.895
7n00rf	93.60	6.15	0.937	88.91	5.22	0.916	96.54	11.44	0.928
7n20rf	93.84	7.39	0.933	90.42	7.76	0.912	93.01	8.75	0.922
7n40rf	93.47	10.36	0.917	87.83	11.76	0.880	87.87	10.58	0.886
Mean	**95.74**	**5.24**	**0.953**	**91.82**	**5.61**	**0.930**	**94.84**	**8.06**	**0.935**

CHAPTER 3

FORWARD PROBLEM

3.1 Introduction

To mathematically explain the electromagnetic phenomena that takes place inside human brain, we will refer to the Maxwell's equations [50].

$$\nabla \times \mathbf{E} = -\frac{\partial \mathbf{B}}{\partial t} \tag{3.1a}$$

$$\nabla \times \mathbf{H} = \mathbf{J} + \frac{\partial \mathbf{D}}{\partial t} \tag{3.1b}$$

$$\nabla \cdot \mathbf{D} = \rho_v \tag{3.1c}$$

$$\nabla \cdot \mathbf{B} = 0 \tag{3.1d}$$

Maxwell's equations are complemented by the following definitions that characterize the medium in which the electromagnetic fields propagate:

$$\mathbf{D} = \varepsilon \mathbf{E} \tag{3.2a}$$

$$\mathbf{B} = \mu \mathbf{H} \tag{3.2b}$$

$$\mathbf{J} = \sigma \mathbf{E} + \mathbf{J_s} \tag{3.2c}$$

In the above equations, $\mathbf{E}$, $\mathbf{D}$, $\mathbf{B}$, $\mathbf{H}$, $\mathbf{J}$, ρ_v are the electric field, electric displacement, magnetic field, magnetic field strength, current density, and free electric charge density respectively. The material dependent parameter ε represents the permittivity, μ represents the permeability and σ represents the conductivity of the medium. Moreover, if we denote $\mathbf{J}$ in Equation (3.2c) as

the total current density produced by the neuronal activity, we may divide it into two components, $\mathbf{J_s}$ and $\sigma\mathbf{E}$. In this case, $\mathbf{J_s}$ corresponds to the primary current, which is introduced by the neural activity within the neuronal cells, and $\sigma\mathbf{E}$ corresponds to the volume current, which is introduced by the effect of the electric field on free charges in the conducting medium.

For biological signals, whose frequency is typically lower than 1 kHz, human body may be considered as an inhomogeneous resistive volume conductor, and electromagnetic fields in a purely resistive volume conductor are assumed to be governed by the quasi-static conditions [47]. Quasi-static conditions eliminate time-varying components of Maxwell equations. Being one of those, $\frac{\partial \mathbf{D}}{\partial t}$ is assumed to be zero inside human body, and consequently:

$$\nabla \cdot \mathbf{J} = 0 \tag{3.3}$$

Using the identity $\mathbf{E}{=}-\nabla\phi$, taking divergence of Equation (3.2c) and substituting it into (3.3), we obtain:

$$\nabla \cdot (\sigma \nabla \phi) = \nabla \cdot \mathbf{J_s} \ in \ \Omega \tag{3.4}$$

Equation (3.4) is the the well known Poisson's equation, and it numerically explains how the voltage initiated by the electrical activities inside a purely resistive volume conductor (Ω) is distributed. At the interface of two different regions, boundary conditions are to be taken into account. Assuming $\delta\Omega$ is the outer surface of Ω, the boundary condition of the EEG forward problem is usually defined as follows [54]:

$$\mathbf{n} \cdot \sigma \nabla \phi = 0 \ \ on \ \delta\Omega \tag{3.5}$$

3.2 Reciprocity

Before discussing about the theory of reciprocity, it is essential to focus on the mathematical description of the neural activities. Neural activities inside the brain are generally modeled as a dipole source. Although there are different descriptions of the dipole sources inside the brain [45, 46, 53], the most common one is made by Brody and Romans in [45]. According to Brody and Romans, the dipole is composed of a current source ($+i$) and a current sink ($-i$), which are separated by a small distance (D) apart. Moreover, the dipole is given a vectorial description of $\boldsymbol{iD}$.

Based on the above description, assume there is a current dipole with strength $\boldsymbol{iD}$ located between $\mathbf{x}$ and $\mathbf{y}$ points (Figure 3.1). This dipole causes a potential difference between $\mathbf{a}$ and $\mathbf{b}$. In the direct approach of the EEG forward problem, the potential distribution due to such current dipoles is solved for several times, which in turn requires a significant amount of computational time and power. Looking at the same problem from a different point of view, this requirement may be eliminated. Introduced into the EEG field by Rush and Driscoll [47], the reciprocity theorem proposes to compute the *lead field*, which is presented as $\nabla\phi_{\mathbf{xy}}$ in (3.6), for every measurement electrode pair. The theorem states that after computing the lead field once, a simple dot product produces the same result with the computation of the forward problem.

The key statement in this theorem is that the voltage difference measured at electrodes $\mathbf{a}$ and $\mathbf{b}$ caused by a dipole source with unity strength is equal to the voltage difference generated at the source point by applying a unit current to the measurement electrodes. We may mathematically explain this statement subject to the Brody and Romans' definition as follows:

$$\phi_{\mathbf{ab}} = \frac{\boldsymbol{iD} \cdot \nabla\phi_{\mathbf{xy}}}{I_{\mathbf{ab}}} \tag{3.6}$$

Lastly, the potential distribution in Figure 3.1b is governed by [54] the Laplace's equation given in (3.7) and by the Neumann boundary condition given in Equation (3.8), which also define the forward problem of Electrical Impedance Tomography (EIT).

$$\nabla \cdot (\sigma \nabla \phi) = 0 \ \textit{inside the volume} \tag{3.7}$$

$$\mathbf{n} \cdot \sigma \nabla \phi = \begin{cases} -I_{\mathbf{ab}} \ at \ \mathbf{a} \\ +I_{\mathbf{ab}} \ at \ \mathbf{b} \\ 0, \ elsewhere \end{cases} \tag{3.8}$$

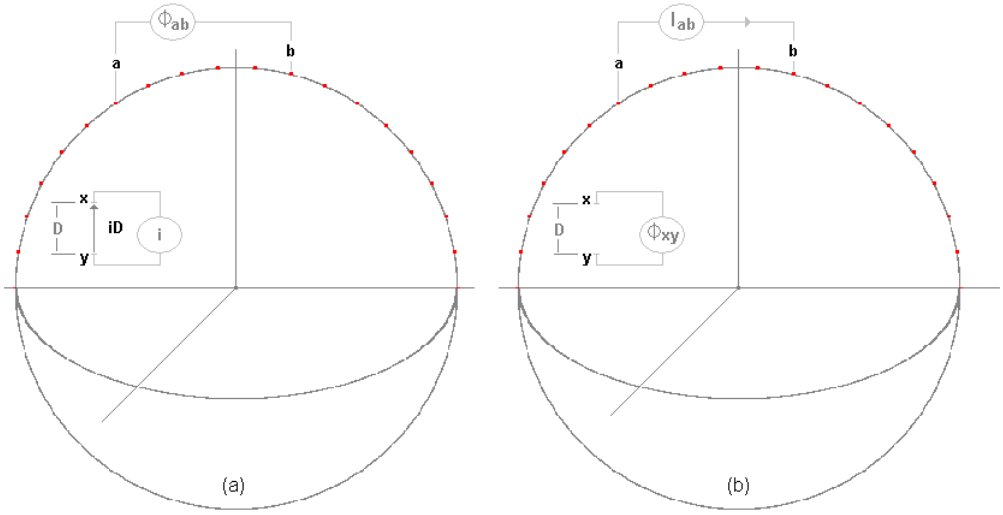

Figure 3.1: The source and measurement-point configuration both in the direct (a) and reciprocal (b) problems.

3.3 Numerical Modeling of the Poisson's Equation

Forward problem of EEG is solving Equation (3.4) in a given volume and with given boundary conditions. For complex geometries, i.e. non-circular or non-elliptical geometries, and for bodies with unevenly distributed inhomogeneities numerical methods have to be employed. In this study the Finite Difference Method (FDM) is chosen as the numerical solver [55]. Defining the divergence of the volume current as I_v, and using the previously given identity $\mathbf{E}{=}{-}\nabla\phi$ yields:

$$\nabla \cdot (\sigma \nabla \phi) = -I_v \tag{3.9}$$

Assuming point sources, I_v may be defined as $I_v = I\delta(r - r_+) - I\delta(r - r_-)$, and placing this definition into (3.9), (3.10) is obtained.

$$\nabla \cdot (\sigma \nabla \phi) = -I\delta(r - r_+) + I\delta(r - r_-) \tag{3.10}$$

Taking the volume integral of (3.10) in the cubic volume shown in Figure 3.2 and using Divergence Theorem, (3.11) is acquired.

$$\iiint_{V_0} \nabla \cdot (\sigma \nabla \phi) dV = \oiint_{S_0} \sigma \nabla \phi \cdot \mathbf{dS} \tag{3.11}$$

In cartesian coordinates, above identity may be decomposed into the following integrals:

$$\begin{aligned} \iiint_{V_0} \{\frac{\partial}{\partial x}(\sigma_0 \frac{\partial \phi}{\partial x}) + \frac{\partial}{\partial y}(\sigma_0 \frac{\partial \phi}{\partial y}) + \frac{\partial}{\partial z}(\sigma_0 \frac{\partial \phi}{\partial z})\} dV = \\ \iint_{front} \sigma_0 \frac{\partial \phi}{\partial x} dydz - \iint_{back} \sigma_0 \frac{\partial \phi}{\partial x} dydz + \\ \iint_{left-side} \sigma_0 \frac{\partial \phi}{\partial y} dxdz - \iint_{right-side} \sigma_0 \frac{\partial \phi}{\partial y} dxdz + \\ \iint_{up} \sigma_0 \frac{\partial \phi}{\partial z} dxdy - \iint_{down} \sigma_0 \frac{\partial \phi}{\partial z} dxdy \end{aligned} \tag{3.12}$$

Among these decomposed integrals, let's just consider the ones related to the x-direction:

$$\iiint_{V_0} \frac{\partial}{\partial x}(\sigma_0 \frac{\partial \phi}{\partial x}) dV = \iint_{front} \sigma_0 \frac{\partial \phi}{\partial x} dydz - \iint_{back} \sigma_0 \frac{\partial \phi}{\partial x} dydz \tag{3.13}$$

By midpoint rule, which states that:

$$\int_d^c \int_b^a f(x, y) dxdy \cong f(\frac{a+b}{2}, \frac{c+d}{2})(a - b)(c - d) \tag{3.14}$$

we may obtain:

$$\iint_{front} \sigma_0 \frac{\partial \phi}{\partial x} dydz \cong h^2 \sigma_0 \frac{\partial \phi}{\partial x} \mid_{x=h/2,\ y=0,\ z=0} \tag{3.15}$$

Now, we will represent this quantity in terms of node voltages. For this purpose, we will refer to boundary conditions, which impose the necessity of continuity in the current flow. Mathematically speaking,

$$\begin{aligned} \sigma_0 \frac{\partial \phi}{\partial x} \mid_{x=\frac{h}{2}^-} &= \sigma_1 \frac{\partial \phi}{\partial x} \mid_{x=\frac{h}{2}^+} \\ \sigma_0 \frac{\phi_{Mx+} - \phi_0}{\partial x} &= \sigma_1 \frac{\phi_1 - \phi_{Mx+}}{\partial x} \end{aligned} \tag{3.16}$$

From Equation (3.16),

$$\phi_{Mx+} = \frac{\sigma_0 \phi_0 + \sigma_1 \phi_1}{\sigma_0 + \sigma_1} \tag{3.17}$$

Representing Equation (3.15) by finite differences and substituting Equation (3.17) into it, we obtain:

$$h^2 \sigma_0 \frac{\partial \phi}{\partial x} \mid_{x=h/2,\ y=0,\ z=0} = \frac{2\sigma_0 \sigma_1 h}{\sigma_0 + \sigma_1} (\phi_1 - \phi_0) \tag{3.18}$$

Following through the same procedure for the second term in (3.13) and introducing the α coefficients as follows:

$$\begin{aligned} \alpha_i &= 2h \frac{\sigma_0 \sigma_i}{\sigma_0 + \sigma_i} \\ \alpha_0 &= \sum_{i=1}^{6} \alpha_i \end{aligned} \tag{3.19}$$

we obtain the finite difference approximation as:

$$\sum_{i=1}^{6} \alpha_i \phi_i - \alpha_0 \phi_0 = -I\delta(r - r_+) + I\delta(r - r_-) \tag{3.20}$$

Filling the system matrix with α coefficients, we obtain the system equation, which may be represented in the form of $\mathbf{x} = \mathbf{A} \cdot \mathbf{b}$. Completing the filling process, the system equation should be solved with an appropriate solver, whose details will be given next.

Before closing the numerical model discussion, an important remark should be made. The differential equations that govern the reciprocal problem of

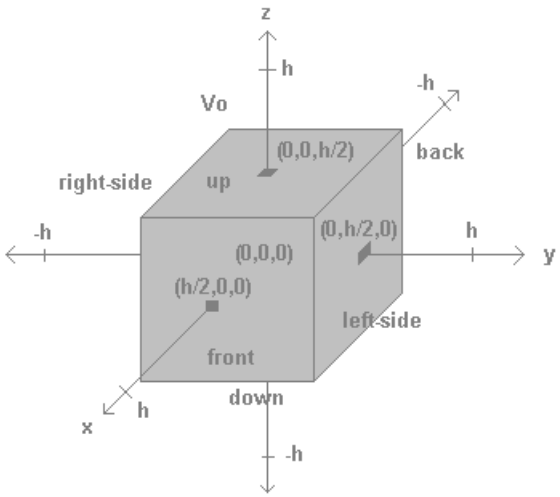

Figure 3.2: Employed finite difference model is composed of equally spaced nodes. The distance between each node is shown as "h". Here you may see a sample node whose location is assumed to be the origin and whose surrounding cubic volume is represented by V_0 [55].

the EEG, and the forward problem of EIT (the lead field problem of EEG) are given in Equations (3.7) and (3.8). While implementing the Neumann boundary condition by the Finite Differences, definition of the surface normal may be problematic. It may be undefined as in the case of the current source & sink nodes shown in Figure 3.3, or it may cause extra computational power demand. To overcome these problems, we employed the same numerical model that we used during the direct approach and assigned applied currents through the midpoint of the nodes. In other words, we followed Equation (3.20) for solving both direct and reciprocal problems.

3.4 System Solution

For selecting a method to solve a system of equations, properties of the system matrix should be investigated first. Looking at the system matrix that is generated by the coefficients of Equation (3.19) in more detail, four important characteristics should be noted:

The first one is sparsity. Due to the nature of finite differences, derivative at a point may be represented by only a limited number of neighbors, and this generates a huge number of zero coefficients in the system matrix. The

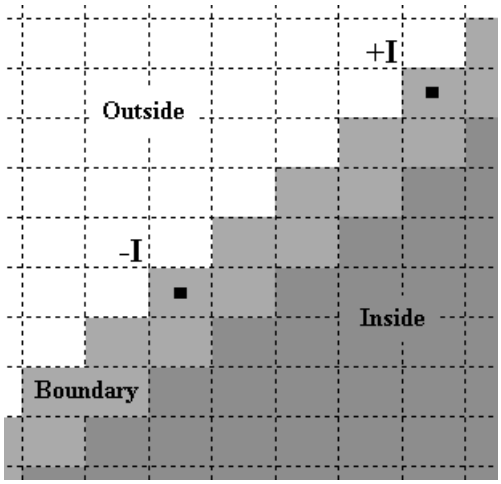

Figure 3.3: Location of current source and sink in the reciprocal problem.

second one is symmetry. The symmetry property arises from the fact that coefficients for two neighbors are identical in their corresponding rows. The third characteristics is directly related to the rank of the system matrix, which is equal to the total number of equations in the system minus one. This fact causes singularity, and systems of equations that have singular system matrices have an infinite number of solutions. Finally, the fourth characteristics, as shown by Mohr and Vanrumste [60], is that the system matrix is positive semi-definite.

For the solution of such equations, where the system matrix is sparse, symmetric, singular and positive semi-definite, it is practical to employ iterative methods. As the name implies, iterative methods try to estimate the solution to a linear system of equations iteratively. At each step, an estimation is generated by previous estimates or previous residuals or both. Investigating previous estimates or residuals, a new search direction is determined and another estimation is created. This recursive procedure continues until a predefined iteration number is reached or until a predefined residual is obtained.

In this study, two different iterative methods, Successive Overrelaxation (SOR) and Conjugate Gradients (CG), are employed; their computational power and memory requirements are investigated. With this investigation we checked the feasibility of Finite Difference Method as a numerical solver in the EEG forward problem.

SOR [59] is based on the well-known Gauss-Seidel method, where the computations are performed in a serial fashion, and consequently each new variable update depends on the previous variables' updates. Not allowing simultaneous renewals, both SOR and Gauss-Seidel methods depend on the ordering of the equations. This property gains critical importance in sparse systems, because presence of zeros may drastically change effect of nonzero coefficients. Consequently, the rate of convergence is affected, as well. Successive Overrelaxation method incorporates an extrapolation variable through which weighted average of Gauss-Seidel iterate and previous iterate is taken. This variable aims at increasing the convergence rate, but it is not possible to compute the optimum extrapolation degree in advance. As Mohr and Vanrumste [60] highlighted, in our Finite Difference system different extrapolation degrees produce different solutions. However, all those solutions differ only by an additive constant. Investigating pseudo-code of SOR in Figure 3.4, it is seen that only two vectors of length N (number of unknowns) and the system matrix need to be stored in memory. Regarding the distribution of operations per iteration, only one SAXPY, i.e. Scalar Alpha X Plus Y, (line 12) and one matrix-vector product is required.

CG [59] differs from Successive Overrelaxation method mainly in update methodology. Former method involves adaptive information, by which estimations to the exact solution are generated. Following estimations, corresponding residuals are computed. Lastly, based on estimations and residuals new search directions are determined. Investigating pseudocode of CG in Figure 3.5, we can see that 5 vectors of length N (number of unknowns) and the system matrix is to be stored in memory. As far as operations per iteration is concerned, two inner products (lines 3,11), three SAXPY (lines 8,12,13) and one matrix-vector product (line 10) have to be taken at each step.

Despite higher memory requirement and higher processing power demand, in this study CG is preferred to SOR, because CG necessitate no parameter estimation and converges to more desirable solutions.

1: For some initial guess $x^{(0)}$
2: **for** $k = 1, 2...$ **do**
3: **for** $i = 1, 2, ..., n$ **do**
4: $\sigma = 0$
5: **for** $j = 1, 2, ..., i - 1$ **do**
6: $\sigma = \sigma + a_{(i,j)}\ x_j^k$
7: **end for**
8: **for** $j = i + 1, ..., n$ **do**
9: $\sigma = \sigma + a_{(i,j)}\ x_j^{(k-1)}$
10: **end for**
11: $\sigma = (b_i - \sigma)/a_{(i,i)}$
12: $x_i^k = x_i^{(k-1)} + \omega(\sigma - x_i^{(k-1)})$
13: **end for**
14: Check convergence, continue if necessary
15: **end for**

Figure 3.4: Successive Overrelaxation Method [59]. It is used for solving equations in the form of $\mathbf{A} \cdot \mathbf{x} = \mathbf{b}$. $a_{(i,j)}$, x_i, b_i, w, σ are entity of a square $\mathbf{A}$ matrix, entity of $\mathbf{x}$ vector, entity of $\mathbf{b}$ vector, user specific relaxation factor and a temporarily utilized variable respectively.

1: Compute $r^{(0)} = b - Ax^{(0)}$ for some initial guess $x^{(0)}$
2: **for** $i = 1, 2...$ **do**
3: $\rho_{(i-1)} = r^{(i-1)^T} r^{(i-1)}$
4: **if** i=1 **then**
5: $p^{(1)} = r^{(0)}$
6: **else**
7: $\beta_{(i-1)} = \rho_{(i-1)}/\rho_{(i-2)}$
8: $p^{(i)} = r^{(i-1)} + \beta_{(i-1)} p^{(i-1)}$
9: **end if**
10: $q^{(i)} = Ap^{(i)}$
11: $\alpha_{(i)} = \rho_{(i-1)}/p^{(i)^T} q^{(i)}$
12: $x^{(i)} = x^{(i-1)} + \alpha_{(i)} p^{(i)}$
13: $r^{(i)} = r^{(i-1)} + \alpha_{(i)} q^{(i)}$
14: Check convergence, continue if necessary
15: **end for**

Figure 3.5: Conjugate Gradient Method [59]. It is used for solving equations in the form of $\mathbf{A} \cdot \mathbf{x} = \mathbf{b}$. $a_{(i,j)}$, x_i, b_i are entity of a square $\mathbf{A}$ matrix, entity of $\mathbf{x}$ vector and entity of $\mathbf{b}$ vector respectively. r, α, β, p, q and ρ are all temporarily utilized variables.

3.5 Validation of the Numerical Model

The accuracy rate of the numerical model is tested on both EEG and EIT forward problems. EIT forward problem is included into the validation process, because reciprocal EEG forward problem is analogous to the EIT forward problem. The accuracy rates are determined by using Relative Difference Measure (RDM) and RDM* metrics [49].

$$\%RDM = \sqrt{\frac{\sum_{i=1}^{N}(V_{a_i} - V_{n_i})^2}{\sum_{i=1}^{N}(V_{a_i})^2}} \text{ x } 100 \tag{3.21}$$

$$RDM^* = \sqrt{\sum_{i=1}^{N}\left(\frac{V_{a_i}}{\sqrt{\sum_{i=1}^{N}(V_{a_i})^2}} - \frac{V_{n_i}}{\sqrt{\sum_{i=1}^{N}(V_{n_i})^2}}\right)^2} \tag{3.22}$$

In (3.21) and (3.22), V_a represents the analytical solution, V_n represents the numerical solution, and N represents the number of test points.

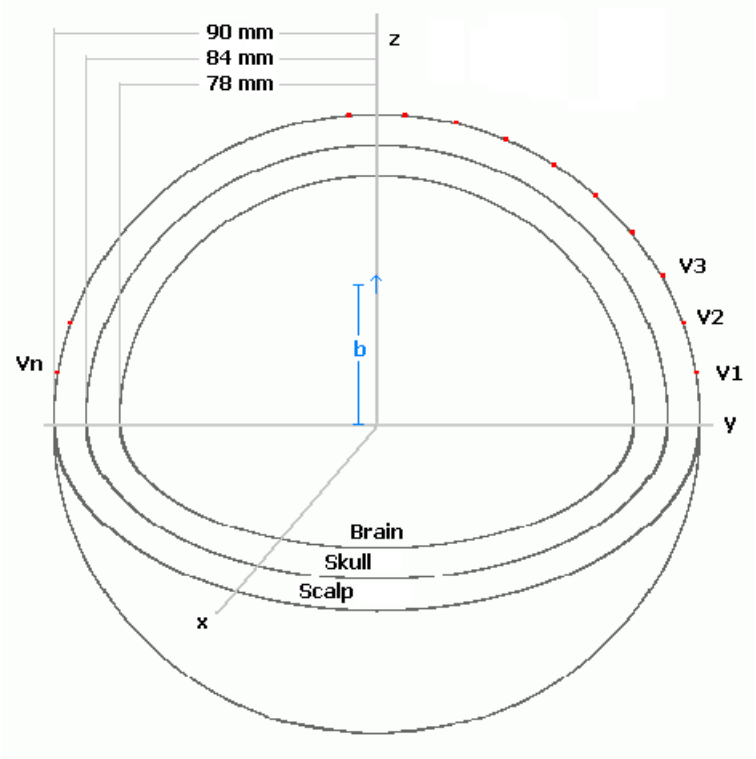

Figure 3.6: Geometry on which EEG and 3D EIT forward problems are solved both analytically and numerically.

3.5.1 EEG Forward Problem with the Direct Approach

EEG forward problem is solved analytically [48] and numerically by the direct approach for a spherical geometry shown in Figure 3.6. The spherical volume is composed of three shells, representing brain, skull and scalp tissues. Brain and scalp tissue conductivities are assumed to be equal and skull conductivity is chosen as (i) same as soft tissue conductivity (ii) 1/15th of the soft tissue conductivity [52] and (iii) 1/80th of the soft tissue conductivity [47]. Numerically computed voltages at nodes on the upper surface are compared with the analytical ones, and results of this test is presented in Figure 3.7. In addition, effect of inter-node spacing is investigated, as well. For a skull conductivity / soft tissue conductivity ratio of 15, forward problem is solved numerically for 10 tangential and for 10 radial dipoles at 1mm, 2mm, 3mm and 6mm node resolutions. Results of this tests are presented in Figures 3.8 and 3.9.

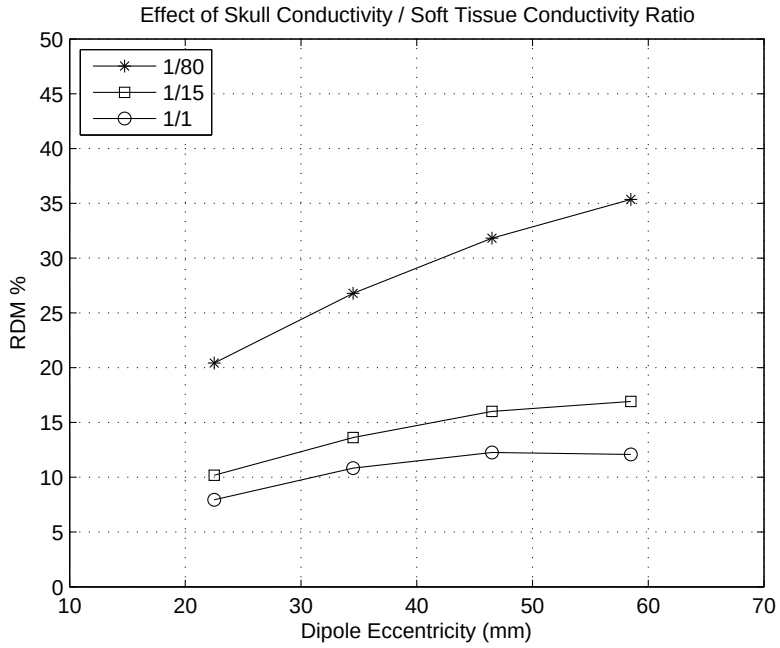

Figure 3.7: %RDM values due to a radial dipole at varying eccentricities and skull conductivity / soft tissue conductivity ratios. The inter-node spacing is selected as 1mm.

Based on Figure 3.7, we may conclude that the numerical solution deviates from the correct solution with increasing skull conductivity / soft tissue

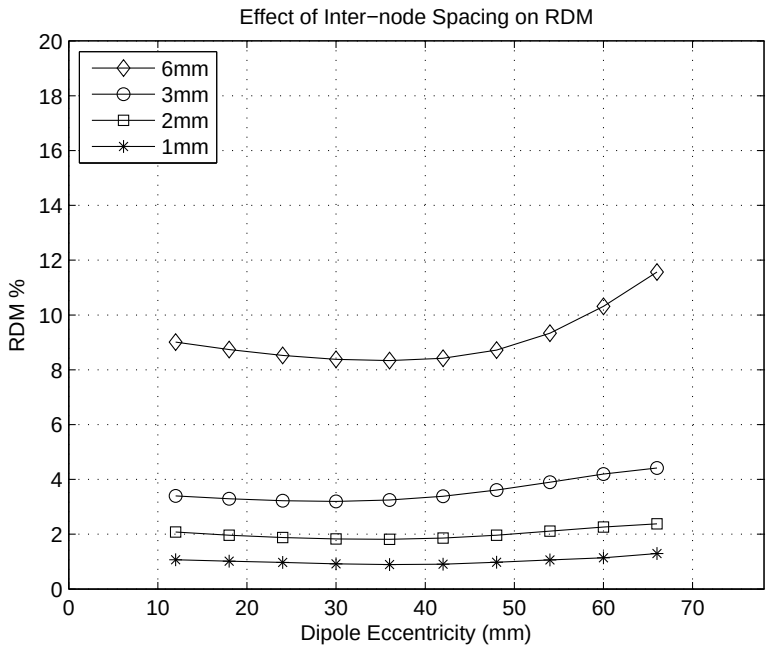

Figure 3.8: %RDM values due to 10 tangential dipoles at varying eccentricities and inter-node spacings. The skull conductivity / soft tissue conductivity ratio is assumed to be 15 [52].

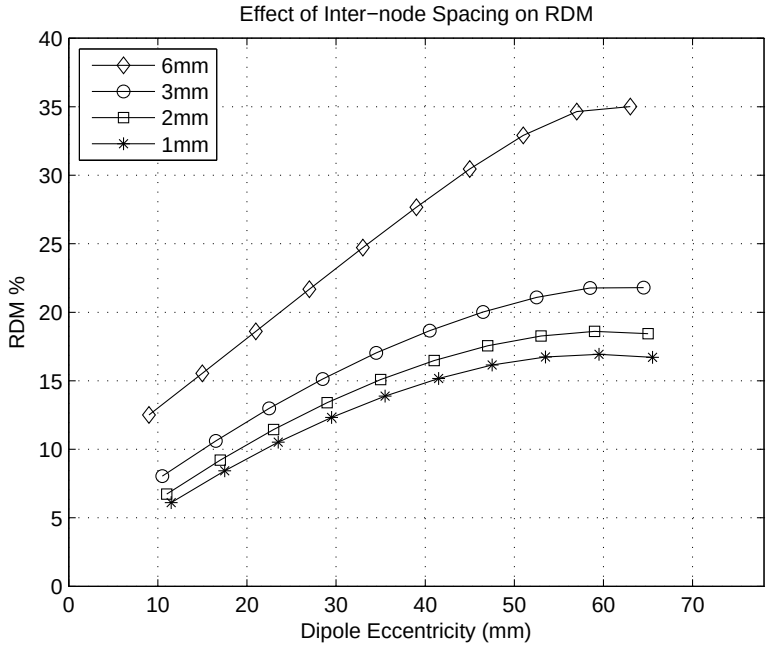

Figure 3.9: %RDM values due to 10 radial dipoles at varying eccentricities and inter-node spacings. The skull conductivity / soft tissue conductivity ratio is assumed to be 15 [52].

conductivity ratio. As the conductivity difference between hard tissue and its neighboring regions increases, the potential distribution shows great alterations at the interfaces, and the numerical solution becomes unable to follow it. Moreover, Figures 3.8 and 3.9 show us that the distance between two FD nodes has also great importance. Employing closer nodes yields more accurate results. However, we realized that the improvement in the numerical results saturate after some point, and it might not be feasible to decrease the internode spacing too much.

3.5.2 EIT Forward Problem

For the EIT forward problem, 2D circular and 3D spherical geometries are chosen. Analytical solution of the 2D EIT forward problem, for both homogeneous and inhomogeneous cases, are obtained by solving Poisson's equation subject to the governing boundary conditions (see Appendix A for details on the analytical solution). Analytical solutions of the 3D homogeneous and inhomogeneous EIT forward problems are obtained from [47]. Results of related tests are given in Tables (3.1) to (3.4).

Table 3.1: %RDM and RDM* values for the 2D EIT forward problem, which is solved for a disk with 90mm radius. The disk is assumed to have homogeneous conductivity.

Internode Spacing(mm)	**RDM(%)**	**RDM***
1.0	1.66	0.015
2.0	3.21	0.029
3.0	4.54	0.040
5.0	7.14	0.063
6.0	8.21	0.071

Table 3.2: %RDM and RDM* values for the 2D EIT forward problem, which is solved for a disk with 90mm radius. The disk has a concentric inhomogeneity with a radius of 60mm.

Internode Spacing(mm)	**RDM(%)**	**RDM***
1.0	0.89	0.008
2.0	1.61	0.014
3.0	2.56	0.018
5.0	3.83	0.033
6.0	5.00	0.044

Table 3.3: %RDM and RDM* values for the 3D EIT forward problem, which is solved for a sphere with 90mm radius. The sphere is assumed to have homogeneous conductivity. The measurement is made at spherical region of 78mm radius.

Internode Spacing(mm)	**RDM(%)**	**RDM***
2.0	3.54	0.013
3.0	4.88	0.018
6.0	10.07	0.035

Table 3.4: %RDM and RDM* values for the 3D EIT forward problem, which is solved for a sphere with 90mm radius. The sphere has concentric inhomogeneities with 84mm and 78mm radii. The comparison is made only at the inner-most region. Region conductivities have a ratio of 15:1:15.

Internode Spacing(mm)	**RDM(%)**	**RDM***
2.0	3.01	0.012
3.0	5.49	0.022
6.0	11.66	0.049

3.5.3 EEG Forward Problem with the Reciprocal Approach

Validation of the reciprocal approach is of highest importance throughout the evaluation process of the numerical method, because it is this approach that will be employed later on the inverse problem solution, and consequently in the electrical source localization. The reciprocal approach is evaluated by solving EEG forward problem analytically [48], by solving EIT forward problem numerically and by applying Equation (3.6) accordingly. The procedure is repeated for varying radial dipole positions on a spherical geometry shown in Figure 3.6. Two electrodes on the y-plane are selected as test electrodes. One of these electrodes makes 30 degrees, and the other one makes 120 degrees with the y-axis. The first electrode is selected as a unit current source, and the latter is selected as a unit current sink. The internode spacing is selected as 1mm, 2mm, 3mm and 6mm. Number of corresponding grid nodes over which the potential distribution is solved may be seen in Table (3.5). In Table (3.5), the average matrix filling time and the average system solution time for an Intel Core2Duo 2.66 GHz CPU with 2 GB RAM of computer are also given. The actual potential difference between the test electrodes, which is calculated by the analytical method, and the estimated one by the reciprocal approach are compared and the RDM value is computed. These RDM values are presented in Figure 3.10 and in Figure 3.11.

Table 3.5: Number of grid nodes, average time required for matrix filling and average time required for system solution at varying internode spacing values are given. The average durations are based on implemented MATLAB® source code run on an Intel Core2Duo 2.66 GHz CPU with 2 GB RAM of PC.

Internode Spacing	**Total number of grid nodes**	**Average matrix filling time**	**Average system solution time**
6mm	16,567	0.05 sec	0.10 sec
3mm	121,769	0.38 sec	2.64 sec
2mm	401,735	1.30 sec	14.92 sec
1mm	3,130,725	31.32 sec	520.23 sec

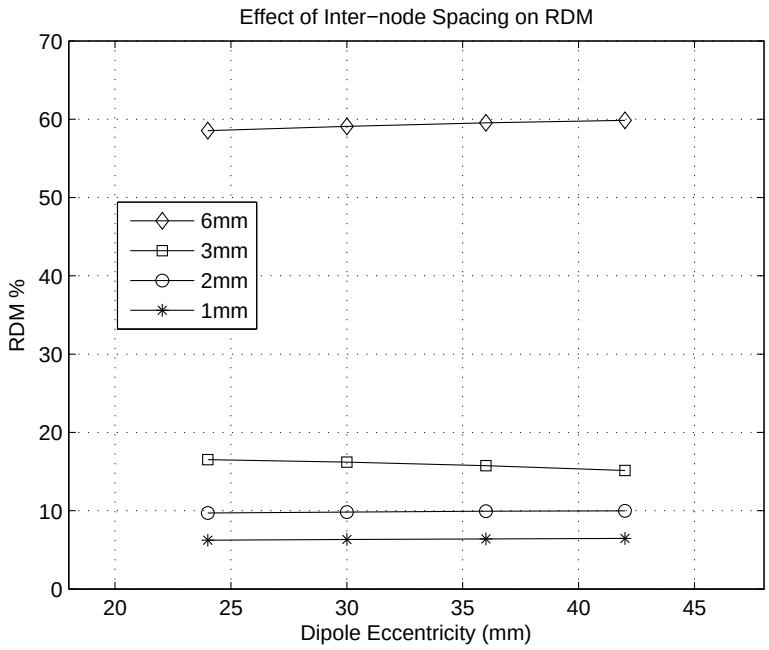

Figure 3.10: RDM values due to a radial dipole at varying eccentricities and inter-node spacings. The skull conductivity / soft tissue conductivity ratio is assumed to be 15 [52].

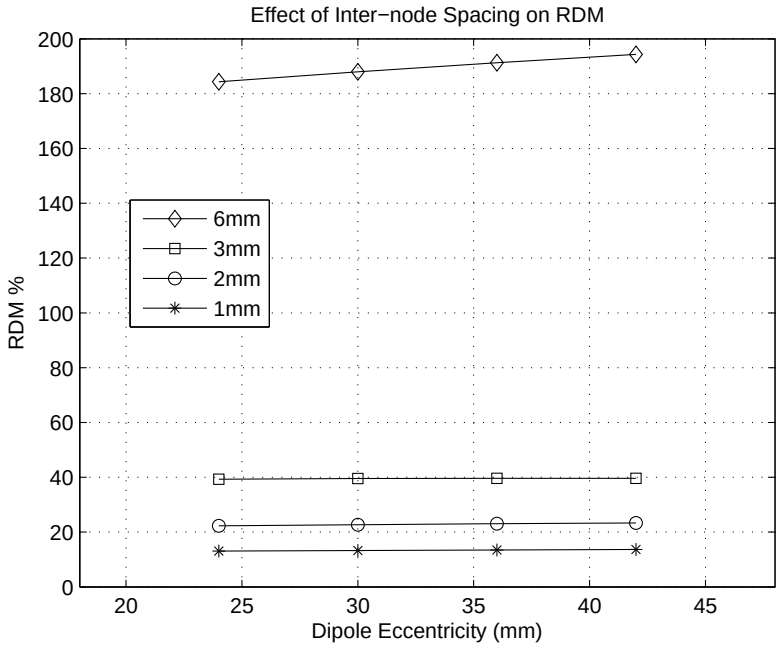

Figure 3.11: RDM values due to a radial dipole at varying eccentricities and inter-node spacings. The skull conductivity / soft tissue conductivity ratio is assumed to be 80 [47].

3.5.4 Comparison of Direct and Reciprocal Approaches

To be able to compare direct and reciprocal approaches correctly, aforementioned test results are not satisfactory, because the number and location of test points are not the same. To eliminate this drawback, one last validation step is added into the study. The reciprocal approach for the EEG forward problem is analyzed by first selecting two electrodes on the spherical geometry shown in Figure 3.6 and then computing the RDM value for radial and tangential dipoles with different eccentricities. The dipoles are moved from 12mm up to 66mm. Without changing the location of selected electrodes and selected dipole eccentricities, the RDM value of the numerical method that follows the direct technique is calculated as well, and the results are presented along with the ones of reciprocal technique.

Table 3.6: Reciprocal and direct approaches are compared based on %RDM values calculated for 10 tangential dipoles and one specific electrode pair.

Internode Spacing	%RDM for the Reciprocal Approach	%RDM for the Direct Approach
6mm	1.68 %	1.68 %
3mm	2.07 %	2.48 %
2mm	0.88 %	0.86 %
1mm	0.51 %	0.57 %

Table 3.7: Reciprocal and direct approaches are compared based on %RDM values calculated for 10 radial dipoles and one specific electrode pair.

Internode Spacing	%RDM for the Reciprocal Approach	%RDM for the Direct Approach
6mm	57.78 %	57.78 %
3mm	14.60 %	14.60 %
2mm	9.57 %	8.74 %
1mm	4.68 %	4.68 %

Looking at Tables (3.7) and (3.6), some critical observations could be made. The first important point here is that accuracy levels of both reciprocal and direct approaches are very similar. Moreover, at low inter-node spacings the

FD method provides us enough precision during computation of potential distribution. Both statements help us conclude that the FD method based on reciprocal approach might be a feasible choice for source localization procedures. In addition to the direct approach & reciprocal approach comparison, the difference between the RDM values for radial and tangential dipoles takes attention, too. The comparatively high inaccuracy of radial dipoles stems from the fact that the test electrodes are placed close to the radial axis of the radial dipoles. Since the dot product in Equation (3.6) is expected to be low in those cases, the error becomes high. However, in the case of tangential dipoles, this dot product is high, and consequently lower accuracy is obtained. Lastly, looking at the above tables one more time, one can question why the RDM value for 3mm spacing is higher than the one for the 6mm spacing. We believe that this situation is caused by discreet modeling of the test geometry, and it is, therefore, of little importance.

3.6 Solutions on a Realistic Head Model

Formerly described Finite Difference scheme is applied on a realistic head model. To obtain the model, initially head of a healthy subject is scanned in 3D, and axial T1-weighted MR images are acquired using 1.5 T General Electric system with TR=540 ms, TE=12 ms. In-plane-resolution is chosen as about 1 cm, which corresponds to 256x256 image size, and out-of-plane resolution is chosen as about 3 cm, which corresponds to 72 slices. Following acquisition, the volume is segmented into 7 compartments (air, scalp, skull, eyeballs, cerebrospinal fluid, gray matter and white matter) automatically by the software whose theatrical principles are given in the previous chapter. One axial and one coronal slice of the segmented volume may be seen in Figure 3.12. (At this point please note that in-plane-resolution is about one third of out-of-plane resolution, and therefore, the staircase affect is much more evident on the coronal view) We have assigned homogeneous conductivity values into each voxel. Values are selected from [56] and are listed in Table (3.8). Finally, we placed radial and tangential dipoles at two different depths one by one.

The difference between deep and shallow dipoles are around 6 cm, and the shallow dipole is around 3.6 cm below the brain surface. Resultant voltage distributions as seen from the inner half and upper scalp are presented in Figure 3.14.

Table 3.8: Homogeneous tissue conductivities [56]

Compartment	Conductivity $(\Omega m)^{-1}$
Air	0.0000
Scalp	0.2725
Skull	0.0132
Eyeballs	0.5000
CSF	1.7900
GM	0.3300
WM	0.2000

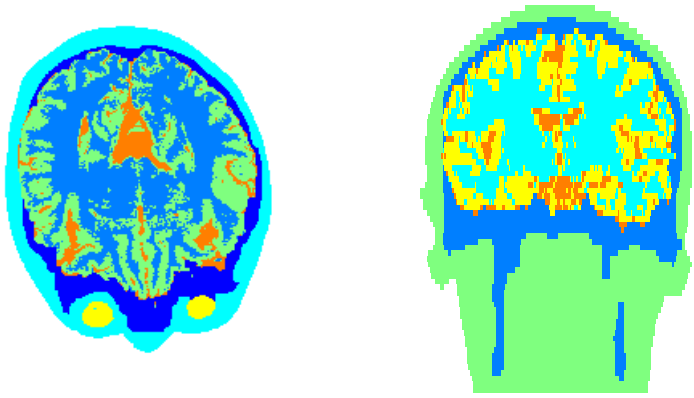

(a) (b)

Figure 3.12: Realistic model (a) Axial view (b) Coronal view

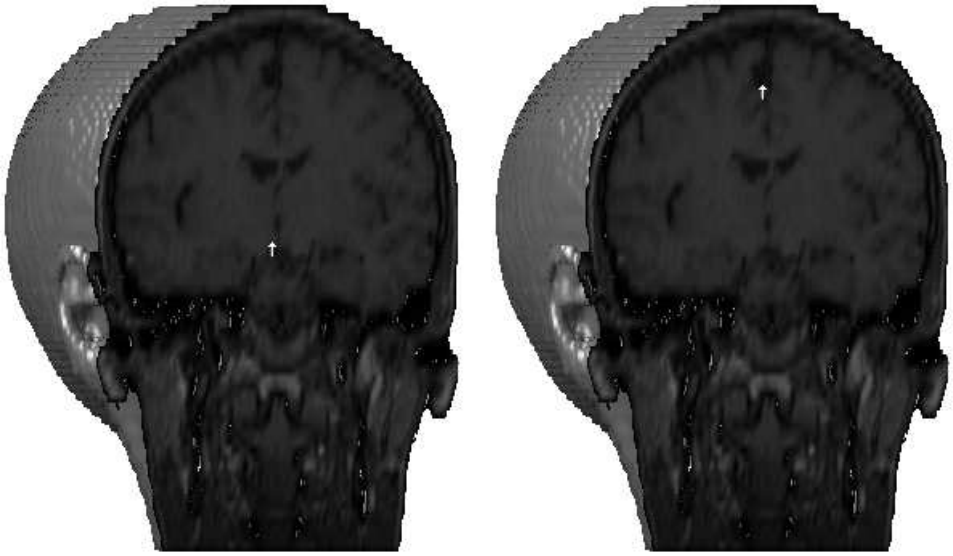

(a) (b)

Figure 3.13: (a) Radial dipole about 9.6 cm below the scalp (b) Radial dipole about 3.6 cm below the scalp

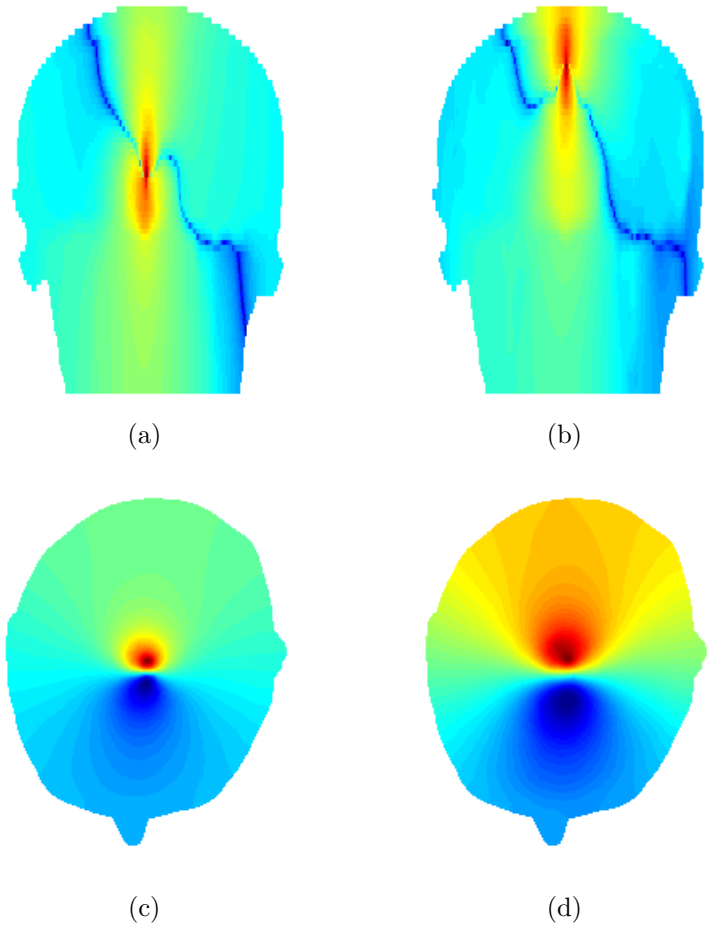

Figure 3.14: (a) Absolute value of the voltage distribution inside human head due to a radial dipole placed about 9.6 cm below the scalp (b) Absolute value of the voltage distribution inside human head due to a radial dipole placed about 3.6 cm below the scalp (c) Scalp voltage distribution due to a tangential dipole placed at a deep location (d) Scalp voltage distribution due to a tangential dipole placed at a near surface location

CHAPTER 4

CONCLUSIONS

This study focuses on three main points: The first one is segmentation of Magnetic Resonance (MR) images into cerebrospinal fluid, gray matter, white matter, eye, skull and scalp tissues. A general framework is created for this purpose, and tissue-specific segmentation methods are selected and implemented accordingly. During segmentation process, only T1-weighted images are used, because compared to dual-spin echo (i.e., PD- and T2-weighted) imaging its acquisition time is shorter, signal-to-noise ratio (SNR) is higher, intensity non-uniformity is less and also possibility of motion artifacts is lower [24].

Among the tissues listed above, skull represents the major difficulty in the whole segmentation process. The reason is that skull has a very low intensity at MR images and often tends to be misclassified as air. However despite this difficulty, we avoided employing Computerized Tomography (CT) images in this study to protect patients from X-ray exposure and to refrain from registration problem.

Applied segmentation methods are tested on synthetic MR data, whose ground truth is available. Tests are carried out under different noise levels. Quantitative analysis of brain segmentation procedure showed that the overlapped region ratio between ground truth and automatic segmentation is in average 89.15%; mean RDM value for intensity non-uniformity correction procedure is 1.36%, and lastly, minimum mean ratio of overlapped region for brain tissue classification procedure is 91.82%. These results prove that selected algorithms provide us with a satisfactory amount of accuracy.

Regarding the future of MRI segmentation studies, there are two different approaches that need attention most. One of these two main concepts is implanting MR physics into the algorithm, so that resistance to acquisition parameter variance is obtained [43]. The other concept is investigating available MR protocols and determine the most appropriate one for tissue specific delineation [44].

The second focus of interest in this thesis study was using the Finite Difference Method (FDM) in the forward problem of Electroencephalography (EEG). We implemented a successful FD scheme, and validated its accuracy rate on the direct approach. For a skull conductivity / soft tissue conductivity ratio of 15 [52], 13.29 % mean RDM, 0.0613 RDM* is obtained for 10 radial dipoles, and 1.02 % mean RDM, 0.0091 RDM* is obtained for 10 tangential dipoles located from 12mm to 66mm above origin. We realized that FDM solves the forward problem accurately, and the accuracy increases with decreasing internode spacing. However, we also realized that the improvement in the accuracy saturates with decreasing of internode spacing. Based on our experiments, dividing the problem geometry into 400,000 grid nodes is a feasible choice in terms of computational load versus correctness balance.

The third and a critical focus of interest of this study was application of reciprocity with the FD method in EEG forward problem. Since the Electrical Impedance Tomography (EIT) forward problem and the reciprocal problem of EEG show great analogy, we included EIT forward problem into the validation process, and the test geometry along with the results are given in Tables (3.1) to (3.4). Moreover, the accuracy rate of the reciprocal approach is measured for a single electrode pair, as well. The main conclusion that may be reached by Table (3.5), Figure 3.10 and Figure 3.11 is that 1mm of internode spacing value produces a highly accurate estimate in less than 10 minutes. Even for a skull conductivity / soft tissue conductivity ratio of 80 [47], a mean RDM value of 10.99 % is obtained at 1mm internode spacing, which in turn necessitates calculation of potential distribution on 3,130,725 numbers of grid nodes. This mean RDM value is computed at 4 different radial dipole locations.

Before making a final statement on the comparison of direct and reciprocal approaches, we made one more test on the same geometry shown in Figure 3.6. Selecting two specific electrodes and 10 radial, 10 tangential dipoles, we computed the error rates for both approaches and realized that they generate almost the same and considerably low RDM values. Considering the main goal of source localization, which requires solving the inverse problem either by successive forward problem solutions or by reciprocal problem solutions, we concluded that the FD method with the reciprocal approach is capable of fulfilling this task by a significant amount of accuracy. The RDM value of the reciprocal approach is determined as 4.68 % for 10 radial dipoles, and 0.51 % for 10 tangential dipoles. This accuracy is achieved by 1 mm of internode distance. One more critical remark here to be made is the change in the error rate with respect to the grid spacing. Figures 3.10 and 3.11 reveal that the error increases exponentially with decreasing number of FD nodes.

We also evaluated the memory requirement and complexity of adapted FD scheme. Best method for evaluating the general scheme is to investigate the procedure used for solving the system equation. We compared Conjugate Gradients (CG) and Succesive Overrelaxation (SOR) procedures for this purpose, and based on this comparison we favored CG over SOR, because CG does not require any parameter estimation and converges more acceptable solutions. Looking into CG in more detail, it may be showed that number of operations per iteration is 2 inner products, 3 SAXPY and one matrix-vector product. Moreover, the memory requirement is 5 times the number of unknowns, which do not create a problem for current computer systems.

REFERENCES

[1] Baillet S., Mosher J.C. and Leahy R.M., "Electromagnetic Brain Mapping", *IEEE Signal Processing Magazine*, 2001, 18(6):14-30

[2] Baillet S. and Garnero L., "A Bayesian Approach to Introducing Anatomo-Functional Priors in the EEG/MEG Inverse Problem", *IEEE Transactions on Biomedical Engineering*, 1997, 44(5):374-385

[3] Roth B.J., Balish M., Gorbach A. and Sato S., "How Well does a Three-sphere Model Predict Positions of Dipoles in a Realistically Shaped Head?", *Electroencephalography Clinical Neurophysiology*, 1993, 87(4):175-184

[4] Cuffin B.N., "EEG Localization Accuracy Improvements Using Realistically Shaped Head Models", *IEEE Transactions on Biomedical Engineering*, 1996, 43(3):299-303

[5] Huiskamp G., Vroeijenstijin M., van Dijk R., Wieneke G. and van Huffelen A.C., "The Need for Correct Realistic Geometry in the Inverse EEG Problem", *IEEE Transactions on Biomedical Engineering*, 1999, 46(11):1281-1287

[6] Akalin-Acar Z. and Gencer N.G., "An Advanced Boundary Element Method (BEM) Implementation for the Forward Problem of Electromagnetic Source Imaging", *Physics in Medicine and Biology*, 2004, 49:5011-5028

[7] Gencer N.G. and Akalin-Acar Z., "Use of the Isolated Problem Approach for Multi-Compartment BEM Models of Electro-Magnetic Source Imaging", *Physics in Medicine and Biology*, 2005, 50:30073022

[8] Gonzales R.C. and Woods R.E., "Digital Image Processing (2nd edition)", Addison-Wesley, March, 1992

[9] Sahoo P.K., Soltani S., Wong A.K.C. and Chen Y.C., "A Survey of Thresholding Techniques", *Computer Vision, Graphics, and Image Processing*, 1988, 41(2):233-260

[10] Kass M., Witkin A. and Terzopoulos D., "Snakes: Active Contour Models", *International Journal of Computer Vision*, 1988, 1(4):321-331

[11] Cohen L.D., "On Active Contour Models and Balloons", *CVGIP: Image Understanding*, 1991, 53(2):211-218

[12] Xu C. and Prince J.L., "Snakes, Shapes and Gradient Vector Flow", *IEEE Transactions on Image Processing*, 1998, 7(3):359-369

[13] Xu C. and Prince J.L., "Gradient Vector Flow Deformable Models", *Handbook of Medical Imaging*, edited by Isaac Bankman, Academic Press, September, 2000

[14] Duda R.O., Hart P.E. and Stork D.G., "Pattern Classification (2nd edition)", Wiley Interscience, November, 2000

[15] Perona P. and Malik J., "Scale-Space and Edge Detection Using Anisotropic Diffusion", *IEEE Transactions on PAMI*, 1990, 12(7):629-639

[16] Gerig G., Kubler O., Kikinis R. and Jolesz F.A., "Nonlinear Anisotropic Filtering of MRI Data", *IEEE Transactions on Medical Imaging*, 11(2):221-232

[17] Ségonne F., Dale A.M., Busa E., Glessner M., Salat D., Hahn H.K. and Fischl B., "A Hybrid Approach to the Skull Stripping Problem in MRI", *NeuroImage*, 2004, 22(3):1060-1075

[18] Smith S.M., "Fast Robust Automated Brain Extraction", *Human Brain Mapping*, 2002, 17(3):143-155

[19] Stokking R., Vincken K.L. and Viergever M.A., "Automatic Morphology-Based Brain Segmentation (MBRASE) from MRI-T1 Data", *NeuroImage*, 2000, 12(6):726-738

[20] MacDonald D., Kabani N., Avis D. and Evans A.C., "Automated 3-D Extraction of Inner and Outer Surfaces of Cerebral Cortex from MRI", *NeuroImage*, 2000, 12(3):340-356

[21] Tang H., Wua E.X., Mab Q.Y., Gallagherc D., Pereraa G.M. and Zhuangd T., "MRI Brain Image Segmentation by Multi-Resolution Edge Detection and Region Selection", *Computerized Medical Imaging and Graphics*, 2000, 24(6):349-357

[22] Lemieux L., Hagemann G., Krakow K. and Woermann F.G., "Fast, Accurate, and Reproducible Automatic Segmentation of the Brain in T1-Weighted Volume MRI Data", Magnetic Resonance in Medicine, 1999, 42:127-135

[23] Atkins M.S. and Mackiewich B.T., "Fully Automatic Segmentation of the Brain in MRI", *IEEE Transactions On Medical Imaging*, 1998, 17(1):98-107

[24] Arnold J.B., Liow J.S., Schaper K.A., Stern J.J., Sled J.G., Shattuck D.W., Worth A.J., Cohen M.S., Leahy R.M., Mazziotta J.C. and Rottenberg D.A., "Qualitative and Quantitative Evaluation of Six Algorithms for Correcting Intensity Nonuniformity Effects", *NeuroImage*, 2001, 13(5):931-943

[25] Vovk U. Pernus F. and Likar B., "MRI Intensity Nonuniformity Correction by Combining Intensity and Spatial Information", *Physics in Medicine and Biology*, 2004, 49(17):4119-4133

[26] Besag J., "On the Statistical Analysis of Dirty Pictures", *Journal of the Royal Statistical Society. Series B*, 1986, 48(3):259-302

[27] Zijdenbos A.P., Dawant B.M., Margolin R.A. and Palmer A.C., "Morphometric Analysis of White Matter Lesions in MR Images: Method and Validation", *IEEE Transactions on Medical Imaging*, 1994, 13(4):716-724

[28] Held K., Kops E.R., Krause B.J., Wells W.M., III, Kikinis E. and Müller-Gärtner H.W., "Markov Random Field Segmentation of Brain MR Images", *IEEE Transactions on Medical Imaging*, 1997, 16(6):878-886

[29] Leemput K.V., Maes F., Vandermeulen D. and Suetens P., "Automated Model-Based Tissue Classification of MR Images of the Brain", *IEEE Transactions on Medical Imaging*, 1999, 18(10):897-908

[30] Ashburner J. and Friston K.J., "Voxel Based Morphometry - The Methods", *NeuroImage*, 2000, 11(6):805-821

[31] Zhang Y., Brady M. and Smith S., "Segmentation of Brain MR Images Through a Hidden Markov Random Field Model and The Expectation-Maximization Algorithm", *IEEE Transactions on Medical Imaging*, 2001, 20(1):45-57

[32] Pham D.L., "Spatial Models for Fuzzy Clustering", *Computer Vision and Image Understanding*, 2001, 84:285-297

[33] Shattuck D.W., Sandor-Leahy S.R., Schaper K.A., Rottenberg D.A. and Leahy R.M., "Magnetic Resonance Image Tissue Classification Using a Partial Volume Model", *NeuroImage*, 2001, 13(5):856-876

[34] Marroquin J.L., Vemuri B.C., Botello S., Calderon F. and Bouzas A.F., "An Accurate and Efficient Bayesian Method for Automatic Segmentation of Brain MRI", *IEEE Transactions on Medical Imaging*, 2002, 21(8):934-945

[35] Cocosco C.A., Zijdenbos A.P. and Evans A.C., "A Fully Automatic and Robust Brain MRI Tissue Classification Method", *Medical Image Analysis*, 2003, 7(4):513-527

[36] Yang J., Staib L.H. and Duncan J.S., "Neighbor-Constrained Segmentation with 3D Deformable Models", *Lecture Notes in Computer Science*, 2003, 2732:198-209

[37] Horn B.K.P., "Robot Vision", The MIT Press, March, 1986

[38] Rifai H., Bloch I., Hutchinson S., Wiart J. and Garnero L., "Segmentation of the Skull in MRI Volumes Using Deformable Model and Taking

the Partial Volume Effect into Account", *Medical Image Analysis*, 2000, 4(3):219-233

[39] Dogdas B., Shattuck D.W. and Leahy R.M., "Segmentation of Skull and Scalp in 3D Human MRI Using Mathematical Morphology", *Human Brain Mapping*, 2005, 26(4):273-285

[40] Péchaud M., Jenkinson M. and Smith S., "BET2 - MRI Based Estimation of Brain, Skull and Scalp Surfaces", *FMRIB Technical Report TR06MP1*, 2006

[41] Cocosco C.A., Kollokian V., Kwan R.K.S. and Evans A.C., "BrainWeb: Online Interface to a 3D MRI Simulated Brain Database", *NeuroImage*, 5(4), part 2/4, S425, 1997, Proceedings of 3rd International Conference on Functional Mapping of the Human Brain, Copenhagen, May, 1997

[42] Kwan R.K.-S., Evans A.C. and Pike G.B., "MRI Simulation Based Evaluation of Image-Processing and Classification Methods", *IEEE Transactions on Medical Imaging*, 1999, 18(11):1085-1097

[43] Fischl B., Salat D.H., van der Kouwe A.J.W., Makris N., Segonne F., Quinn B.T. and Dale A.M., "Sequence-Independent Segmentation of Magnetic Resonance Images", *NeuroImage*, 2004, 23:s69-s84

[44] Anbeek P., Vincken K.L., van Bochove G.S., van Osch M.J.P. and van der Grond J., "Probabilistic Segmentation of Brain Tissue in MR Imaging", *NeuroImage*, 2005, 27:795-804

[45] Brody D.A. and Romans W.E., "A Model Which Demonstrates the Quantitative Relationship between the Electromotive Forces of the Heart and the Extremity Leads", *American Heart Journal*, 1953, 45(2):263-76

[46] McFee R. and Johnston F.D., "Electrocardiographic Leads I. Introduction", *Circulation*, 1953, 8:554-568

[47] Rush S. and Driscoll D.A., "EEG Electrode Sensitivity–An Application of Reciprocity", *IEEE Transactions on Biomedical Engineering*, 1969, 16(1):15-22

[48] Kavanagh R.N., Darcey T.M., Lehmann D. and Fender D.H., "Evaluation Methods for Three-Dimensional Localization of Electrical Sources in the Human Brain", *IEEE Transactions on Biomedical Engineering*, 1978, 25(5):421-429

[49] Meijs J.W.H., Weier O.W., Peters M.J. and van Oosterom A., "On the Numerical Accuracy of the Boundary Element Method", *IEEE Transactions on Biomedical Engineering*, 1989, 36(10):1038-1049

[50] Gulrajani R.M., "Bioelectricity and Biomagnetism", Wiley, October, 1998

[51] Fuchs M., Drenckhahn R., Wischmann H.A. and Wagner M., "An Improved Boundary Element Method for Realistic Volume-Conductor Modeling", *IEEE Transactions on Biomedical Engineering*, 1998, 45(8):980-997

[52] Oostendorp T.F., Delbeke J. and Stegeman D.F., "The Conductivity of the Human Skull: Results of In Vivo and In Vitro Measurements", *IEEE Transactions on Biomedical Engineering*, 2000, 47(11):1487-1492

[53] Schimpf P.H., Ramon C. and Haueisen J., "Dipole Models for the EEG and MEG", *IEEE Transactions on Biomedical Engineering*, 2002, 49(5):409-418

[54] Gencer N.G. and Acar C.E., "Use of the Reciprocal Problems in Electro-Magnetic Source Imaging of the Human Brain", *Proceedings of the 25th Annual International Conference of the IEEE EMBS*, 2003, 17-21

[55] Vanrumste B., "EEG Dipole Source Analysis in a Realistic Head Model", *PhD Thesis, Faculty of Engineering, Gent University*, 2001

[56] Nixon J.B., Rasser P.E., Teubner M.D., Clark C.R. and Bottema M.J., "Numerical Model of Electrical Potential Within the Human Head", *International Journal for Numerical Methods in Engineering*, 2003, 56(15):2353-2366

[57] Jing L., Zhu S. and He B., "A Finite Difference Method for Solving the Three-Dimensional EEG Forward Problem", *Proceedings of the 27th Annual International Conference of the IEEE EMBS*, 2005, 1540-1543

[58] Hallez H., Vanrumste B., Hese P.V., D'Asseler Y., Lemahieu I. and de Walle R.V., "A Finite-Difference Method with Reciprocity Used to Incorporate Anisotropy in Electroencephalogram Dipole Source Localization", *Physics in Medicine and Biology*, 2005, 50:3787-3806

[59] Barrett R., Berry M., Chan T.F., Demmel J., Donato J., Dongarra J., Eijkhout V., Pozo R., Romine C. and van der Vorst H.V., "Templates for the Solution of Linear Systems: Building Blocks for Iterative Methods", *SIAM Publications*, 1993

[60] Mohr M. and Vanrumste B., "Comparing Iterative Solvers for Linear Systems Associated with the Finite Difference Discretisation of the Forward Problem in Electro-encephalographic Source Analysis", *Med. Biol. Eng. Comput.*, 2003, 41(1):75-84

APPENDIX A

Analytic Solutions to the Forward Problem of Electrical Impedance Tomography

A.1 Solution for a Two Dimensional Homogeneous Disc

General form of the solution:

$$V(r,\theta) = \sum_{n=0}^{\infty} r^n \{a_n cos(n\theta) + b_n sin(n\theta)\} \tag{A.1}$$

Boundary conditions of the problem:

$$V(r=0,\theta) = 0 \tag{A.2a}$$

$$\sigma \frac{\partial V(r,\theta)}{\partial r}|_{r=R} = J(\theta), \tag{A.2b}$$

where $J(\theta)$ is the applied current density and defined as:

$$J(\theta) = \begin{cases} \dfrac{+I}{R\beta}, & \text{for } \alpha_1 - \frac{\beta}{2} \leq \theta \leq \alpha_1 + \frac{\beta}{2} \\ \dfrac{-I}{R\beta}, & \text{for } \alpha_2 - \frac{\beta}{2} \leq \theta \leq \alpha_2 + \frac{\beta}{2} \\ 0, & \text{elsewhere} \end{cases} \tag{A.3}$$

In the above definition, β represents the angular electrode width. From (A.2a):

$$V(r=0,\theta) = a_0 = 0 \tag{A.4}$$

Therefore, Equation A.1 becomes:

$$V(r,\theta) = \sum_{n=1}^{\infty} r^n \{a_n cos(n\theta) + b_n sin(n\theta)\} \tag{A.5}$$

From (A.2b):

$$J(\theta) = \sigma \sum_{n=1}^{\infty} nR^{n-1} \{a_n cos(n\theta) + b_n sin(n\theta)\} \tag{A.6}$$

Multiplying both sides of (A.6) with cos(mθ) and taking the integral in [0,2π]:

$$\int_0^{2\pi} J(\theta) cos(m\theta) d\theta = \sigma \sum_{n=1}^{\infty} nR^{n-1} \int_0^{2\pi} \{a_n cos(n\theta) + b_n sin(n\theta)\} cos(m\theta) d\theta \tag{A.7}$$

Using definition of J(θ), the left hand side of the above equation may be shown as:

$$\int_0^{2\pi} J(\theta) cos(m\theta) d\theta = \int_{\alpha_1 - \beta/2}^{\alpha_1 + \beta/2} \frac{I}{R\beta} cos(m\theta) d\theta - \int_{\alpha_2 - \beta/2}^{\alpha_2 + \beta/2} \frac{I}{R\beta} cos(m\theta) d\theta$$

$$= \frac{2I}{mR\beta} sin(\frac{m\beta}{2}) [cos(m\alpha_1) - cos(m\alpha_2)] \tag{A.8}$$

Knowing the identities,

$$\int_0^{2\pi} cos(n\theta) cos(m\theta) d\theta = \begin{cases} \pi, & \text{for n = m} \\ 0, & \text{otherwise} \end{cases} \tag{A.9}$$

$$\int_0^{2\pi} sin(n\theta) cos(m\theta) d\theta = 0 \text{ everywhere} \tag{A.10}$$

and combining (A.7) with (A.8) we obtain:

$$a_n = \frac{2I}{\pi\beta\sigma n^2 R^n} sin(n\theta) \{cos(n\alpha_1) - cos(n\alpha_2)\} \tag{A.11}$$

$$b_n = \frac{2I}{\pi\beta\sigma n^2 R^n} sin(n\theta) \{sin(n\alpha_1) - sin(n\alpha_2)\} \tag{A.12}$$

Substituting equations (A.11) and (A.12) into (A.1) yields:

$$V(r,\theta) = \frac{2I}{\pi\beta\sigma} = \sum_{n=1}^{\infty} \frac{r^n sin(n\beta/2)}{n^2 R^n}\{cos(n(\alpha_1 - \theta)) - cos(n(\alpha_2 - \theta))\} \quad \text{(A.13)}$$

A.2 Solution for a Two Dimensional Two Shell Disc with Concentric Inhomogeneity

General form of the solution for the inner shell:

$$V_i(r,\theta) = \sum_{n=1}^{\infty} r^n\{a_n cos(n\theta) + b_n sin(n\theta)\} \quad \text{(A.14)}$$

General form of the solution for the outer shell:

$$\begin{aligned} V_o(r,\theta) = \sum_{n=1}^{\infty}\{&(r^n c_n + r^{-n} d_n)cos(n\theta) + \\ &(r^n e_n + r^{-n} f_n)sin(n\theta)\} \end{aligned} \quad \text{(A.15)}$$

Boundary conditions of the problem:

$$\sigma_o \frac{\partial V_o(r,\theta)}{\partial r}|_{r=R_o} = J(\theta) \quad \text{(A.16a)}$$

$$\sigma_i \frac{\partial V_i(r,\theta)}{\partial r}|_{r=R_i} = \sigma_o \frac{\partial V_o(r,\theta)}{\partial r}|_{r=R_i} \quad \text{(A.16b)}$$

$$V_o(R_i,\theta) = V_i(R_i,\theta), \quad \text{(A.16c)}$$

where $J(\theta)$ is the applied current density and defined as:

$$J(\theta) = \begin{cases} \dfrac{+I}{R_o\beta}, & \text{for } \alpha_1 - \frac{\beta}{2} \le \theta \le \alpha_1 + \frac{\beta}{2} \\ \dfrac{-I}{R_o\beta}, & \text{for } \alpha_2 - \frac{\beta}{2} \le \theta \le \alpha_2 + \frac{\beta}{2} \\ 0, & \text{elsewhere} \end{cases}$$

In the above definition, β represents the angular electrode width. From (A.16a):

$$J(\theta) = \sigma_o \sum_{n=1}^{\infty} n\{(R_o^{n-1}c_n - R_o^{-n-1}d_n)cos(n\theta) + (R_o^{n-1}e_n - R_o^{-n-1}f_n)sin(n\theta)\} \tag{A.17}$$

Multiplying both sides of (A.17) with cos(mθ) and taking the integral in [0,2π]:

$$\begin{aligned}\int_0^{2\pi} J(\theta)cos(m\theta)d\theta = \sigma_0 \sum_{n=1}^{\infty} n \\ \{(R_o^{n-1}c_n - R_o^{-n-1}d_n)\int_0^{2\pi} cos(n\theta)cos(m\theta)d\theta + \\ (R_o^{n-1}e_n - R_o^{-n-1}f_n)\int_0^{2\pi} sin(n\theta)cos(m\theta)d\theta\}\end{aligned} \tag{A.18}$$

Using definition of J(θ), the left hand side of the above equation may be calculated as:

$$\begin{aligned}\int_0^{2\pi} J(\theta)cos(m\theta)d\theta &= \int_{\alpha_1-\beta/2}^{\alpha_1+\beta/2} \frac{I}{R_o\beta}cos(m\theta)d\theta - \int_{\alpha_2-\beta/2}^{\alpha_2+\beta/2} \frac{I}{R_o\beta}cos(m\theta)d\theta \\ &= \frac{2I}{mR_o\beta}sin(\frac{m\beta}{2})[cos(m\alpha_1) - cos(m\alpha_2)] \\ &\triangleq K_m^1\end{aligned} \tag{A.19}$$

Since:

$$\int_0^{2\pi} cos(n\theta)cos(m\theta)d\theta = \begin{cases} \pi, & \text{for n = m} \\ 0, & \text{otherwise} \end{cases}$$

and $\int_0^{2\pi} sin(n\theta)cos(m\theta)d\theta = 0$ everywhere, we come up with the following equation:

$$\begin{aligned}\sigma_o m(R_o^{m-1}c_m - R_o^{-m-1}d_m)\pi = K_m^1 \\ => R_o^m c_m - R_o^{-m}d_m = \frac{K_m^1 R_o}{\sigma_o m\pi}\end{aligned} \tag{A.20}$$

From (A.16b):

$$\sigma_i R_i^m a_m = \sigma_o (R_i^m c_m - R_i^{-m} d_m) \tag{A.21}$$

From (A.16c):

$$Ri^m a_m = R_i^m c_m + R_i^{-m} d_m \tag{A.22}$$

=> From (A.21) and (A.22):

$$(\sigma_i - \sigma_o) R_i^m c_m + (\sigma_i + \sigma_o) R_i^{-m} d_m = 0 \tag{A.23}$$

$$\begin{aligned} => d_m &= \frac{(\sigma_o - \sigma_i) R_i^{2m} c_m}{(\sigma_o + \sigma_i)} \\ &= \mu R_i^{2m} c_m \text{ ,where } \mu \triangleq \frac{(\sigma_o - \sigma_i)}{(\sigma_o + \sigma_i)} \end{aligned} \tag{A.24}$$

Substituting (A.24) into (A.20):

$$R_o^m c_m - R_o^{-m} \mu R_i^{2m} c_m = \frac{K_m^1 R_o}{\sigma_o m \pi}$$

$$=> (R_o^m - R_o^{-m} \mu R_i^{2m}) c_m = \frac{K_m^1 R_o}{\sigma_o m \pi}$$

$$=> \boxed{c_m = \frac{K_m^1 R_o}{(R_o^m - R_o^{-m} \mu R_i^{2m}) \sigma_o m \pi}} \tag{A.25}$$

$$=> \boxed{d_m = \frac{K_m^1 R_o \mu R_i^{2m}}{(R_o^m - R_o^{-m} \mu R_i^{2m}) \sigma_o m \pi}} \tag{A.26}$$

Substituting (A.25) and (A.26) into (A.22):

$$\boxed{a_m = \frac{K_m^1 R_o (1 + \mu)}{(R_o^m - R_o^{-m} \mu R_i^{2m}) \sigma_o m \pi}} \tag{A.27}$$

Multiplying both sides of (A.17) with sin(mθ), taking the integral in [0,2π] and following aforementioned procedure:

$$\boxed{e_m = \frac{K_m^2 R_o}{(R_o^m - R_o^{-m}\mu R_i^{2m})\sigma_o m\pi}} \tag{A.28}$$

$$\boxed{f_m = \frac{K_m^2 R_o \mu R_i^{2m}}{(R_o^m - R_o^{-m}\mu R_i^{2m})\sigma_o m\pi}} \tag{A.29}$$

$$\boxed{b_m = \frac{K_m^2 R_o (1+\mu)}{(R_o^m - R_o^{-m}\mu R_i^{2m})\sigma_o m\pi}} \tag{A.30}$$

where $K_m^2 \triangleq \frac{2I}{mR_o\beta} sin(\frac{m\beta}{2})[sin(m\alpha_1) - sin(m\alpha_2)]$

APPENDIX B

Segmentation Software GUI

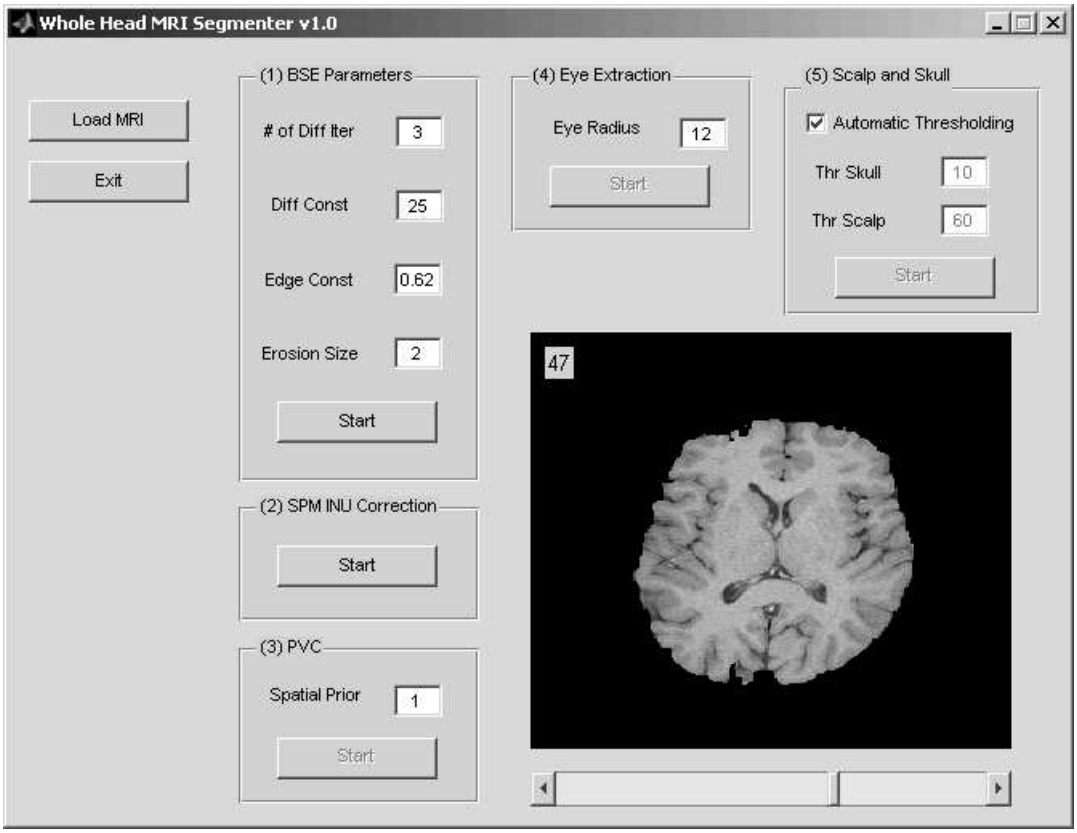

Figure B.1: Whole head MRI segmentation software Graphical User Interface.

During the course of this study, we prepared a MATLAB (Version 7.1.0) ® software for segmenting T1-weighted MR volumes into cerebrospinal fluid (CSF), gray matter (GM), white matter (WM), scalp, skull, and eye-ball tissues. For convenience, a Graphical User Interface (GUI) to the implemented algorithms is created as well (Figure B.1). The graphical interface functions based on the flowchart shown in Figure 2.1.

Initially, an Analyze 7.5 format image volume is loaded into the system by clicking the **Load** button. Loading the input volume, BSE [33] is activated for skull stripping. This module takes 4 inputs. The first one is number of anisotropic diffusion iterations. The second one is diffusion constant. Both variables are adjusted according to the noise level of the input data. For noisy data, number of iterations should be increased. The third parameter is the edge constant used in the Laplacian of Gaussian edge detection, and the last parameter is the size of the structuring element used during erosion operation. Edge detection and erosion steps are quite important for separating brain and surrounding tissues. Deciding on the appropriate parameters skull stripping starts by clicking the **Start** button.

Finalizing skull stripping, intensity non-uniformity (INU) correction module becomes activated. For correcting the INU present in almost all MR images, SPM software package [30] is integrated into the program. This package is capable of computing the Discreet Cosine Transformation coefficients of the non-uniformity field without any user intervention.

After the INU correction step, PVC [33] module becomes activated. The only adjustable parameter here is the spatial prior given in Equation (2.17). It controls the affect of neighbors on the final classification of a voxel. If there is a high amount of noise in the volume, a smaller prior should be selected.

We intuitively selected radius of a human eye as 12mm. Eye segmentation module works according to this assumption. It computes circular Hough transform and located the center of eyes. If another eye radius is to be selected, then **Eye Radius** parameter should be adjusted accordingly.

The final step in the whole head MRI segmentation is the extraction of scalp and skull tissues. At this stage, there are only 2 parameters to be selected. These parameters are intensity threshold values that clamp skull and skull tissues. If the user does not have any prior guess for these thresholds, they could be estimated automatically.